Quaternary Science Reviews 192 (2018) 71–85

Contents lists available at ScienceDirect

Quaternary Science Reviews

journal homepage: www.elsevier.com/locate/quascirev

Younger Dryas to Early Holocene paleoclimate in Cantabria (N Spain): Constraints from speleothem Mg, annual fluorescence banding and stable isotope records

Carlos Rossi [a, *], Petra Bajo [b, c], Rafael P. Lozano [d], John Hellstrom [b]

[a] Dept. Petrología y Geoquímica, Facultad de Ciencias Geológicas, Universidad Complutense, 28040 Madrid, Spain
[b] School of Earth Sciences, The University of Melbourne, Victoria 3010, Australia
[c] School of Geography, The University of Melbourne, Victoria 3010, Australia
[d] Museo Geominero, Instituto Geológico y Minero de España, Ríos Rosas 23, Madrid 28003, Spain

ARTICLE INFO

Article history:
Received 28 January 2018
Received in revised form
14 May 2018
Accepted 20 May 2018
Available online 1 June 2018

Keywords:
Younger dryas
Early holocene
Speleothems
Magnesium concentration
Annual fluorescence lamination
Stable isotopes
Northern Spain

ABSTRACT

The Younger Dryas (YD) stadial represents the most abrupt climate change of the Earth's recent history. Thus, understanding its causes and different local responses is relevant for Quaternary paleoclimatology. We present a speleothem high-resolution proxy record of the Lateglacial to Early Holocene paleoclimate of the Cantabrian Cordillera (N Spain), a strategic location to evaluate the influence of North Atlantic events such as the YD on South-Western Europe. Fluorescence lamination, growth-rate, stable-isotope, and [Mg] records from stalagmite SIR-1 were dated using an age-depth model constrained by U-Th dates and annual-lamina counting. The YD is recorded as a prominent positive $\delta^{13}C$ excursion whose chronology (12.95 ± 0.14 to 11.62 ± 0.16 ka) and shape closely agree with the GS-1 stadial as defined in Greenland ice, supporting the event synchronicity in both areas. A colder and drier YD climate limited soil productivity and dripwater availability, leading to higher $\delta^{13}C$ and [Mg], reduced growth rate, and virtually absent fluorescence lamination. The early YD record (until ~12.5 ka) reflects increasing aridity, whereas the late YD (from ~12.2 ka on) shows the opposite trend. At the YD boundaries, temperature changes influenced the [Mg] record by modifying the Mg partition into calcite. However, this effect was superseded by major changes in dripwater Mg/Ca linked to rainfall variations. During the Early Holocene, the Arnero Sierra was forested and had a relatively warm and humid seasonal climate, indicated in SIR-1 by higher growth rates, lower δ13C and [Mg], and well-developed fluorescent lamination. Similar to other high-resolution stalagmitic records of the Cordillera, from ~8.5 to 8.0 ka SIR-1 reflects a temporary trend of increasing aridity.

© 2018 Elsevier Ltd. All rights reserved.

1. Introduction

In the Northern Hemisphere, the Lateglacial warming was interrupted by a prominent and abrupt cooling event, known as the Younger Dryas (YD) in European terrestrial floral records (e.g. Rach et al., 2014), or Greenland Stadial 1 (GS1) in Greenland ice cores. Because the YD and GS1 boundaries are defined by different criteria, they are not necessarily coincident. However, both correspond to the same event, which, for convenience, will be referred here as the YD. According to the ice-core chronology of Rasmussen et al. (2006), the YD lasted ~1.2 ka, from 12.9 ± 0.14 to 11.7 ± 0.10 ka BP. The YD cooling was restricted to the Northern Hemisphere while the Southern Hemisphere actually experienced warming, pointing to a major disruption of the oceanic thermohaline circulation (Broecker, 1997; De Deckker et al., 2012). This disruption favored the expansion of winter sea-ice in the North Atlantic, cooling adjacent landmasses, and weakened the Asian monsoon (Denton et al., 2005). The YD oceanic re-organization is usually attributed to flooding of the Northern Atlantic by glacial meltwaters from the retreating Laurentide and/or Fennoscandian ice sheets (e.g. Muschitiello et al., 2015). Alternatively, the YD could be part of the sequence of events in transitions from glacial to interglacial climates (Broecker et al., 2010).

The YD represents the most abrupt climate change of the Earth's recent history (Steffensen et al., 2008). Therefore, understanding

* Corresponding author.
E-mail address: crossi@ucm.es (C. Rossi).

https://doi.org/10.1016/j.quascirev.2018.05.025
0277-3791/© 2018 Elsevier Ltd. All rights reserved.

the causes and the different local responses to the YD is highly relevant not only for Quaternary paleoclimatology but also for present-day climate change. In mid-latitude continental regions, speleothems can provide valuable high-resolution proxy records of the YD (e.g. Belli et al., 2013), which have the additional advantage of their potentially precise U-Th chronologies.

The Cantabrian Cordillera of Northern Spain is located strategically to evaluate the influence of North Atlantic climatic events such as the YD on southwestern Europe (Baldini et al., 2015). Some Cantabrian-Cordillera caves developed conditions for speleothem growth during the Lateglacial, including the YD which is recorded in stalagmites from at least two caves near the Atlantic coast (El Pindal and La Garma: Moreno et al., 2010, and Baldini et al., 2015) (Fig. 1). In caves located at moderately higher altitudes in the Cordillera (Fig. 1), published speleothem records normally do not cover the Lateglacial but may include most of the Holocene, such as in Asiul (catchment area: ~300 m a.s.l.; Smith et al., 2016a,b) and Kaite caves (catchment area: ~900 m a.s.l.; Dominguez-Villar et al., 2009). In higher-altitude caves of the Cordillera, calcitic stalagmites apparently only record full interglacial conditions, e.g. in Courel-Sierra caves (catchment area: ~1300 m a.s.l.; Railsback et al., 2017) or Cobre Cave (catchment area: ~1800 m a.s.l.; Muñoz-García et al., 2007) (Fig. 1).

Here, we report a new Lateglacial to Early Holocene speleothem record from a mid-altitude cave in the Cantabrian Cordillera, with particular focus on the YD. We aim (1) to highlight the paleoclimate significance of combining high-resolution Mg concentration data with stable isotopic data, fluorescence imaging, and lamina counting; and (2) to determine the climatic response to the YD climate change in this area from the interpretation of these proxies. This interpretation is based on understanding the main controls on geochemical variability of modern dripwaters and speleothems, obtained in a previous study (Rossi and Lozano, 2016). Given the strategic location of the cave also in terms of altitude (catchment area: ~600 m a.s.l.), we emphasize the comparison to other coeval speleothem records in the region. Such comparison may help to discriminate regional climatic controls from possible local effects.

In stalagmites, variations in Mg concentration along the growth axis are frequently interpreted in terms of paleo-hydrology. During periods of decreasing effective rainfall the residence time of water in the vadose aquifer increases, as reduced water/air ratios in the porosity decrease the relative permeability to water. Due to the slower dissolution kinetics of dolomite relative to calcite, longer water-residence times enhance the release of Mg from dolomite dissolution, increasing Mg/Ca ratios in dripwater and speleothem calcite (Fairchild et al., 2000; Belli et al., 2017). Apart from enhanced water-rock interaction, the precipitation of $CaCO_3$ along vadose flow paths (Prior Calcite Precipitation: PCP) can also increase Mg/Ca ratios during drier climatic conditions (Fairchild et al., 2000; Cruz et al., 2007; Sinclair et al., 2012; Tremaine and Froelich, 2013). PCP preferentially removes Ca^{2+} from solution, increasing its Mg/Ca ratio. It can occur in the cave (e.g. in stalactites) or in other air-filled voids above the cave (Fairchild et al., 2000). Decreasing rainfall enhances PCP partly because such voids become more abundant, and partly because slower drip rates allow more $CaCO_3$ precipitation in stalactites or flowstones (Fairchild and Baker, 2012). Therefore dripwater Mg/Ca is usually controlled by effective rainfall because this influences both water-residence time and PCP (McDonald et al., 2007).

However, apart from drier climate, PCP-related increases in dripwater Mg/Ca can respond to higher supersaturations linked to enhanced ventilation (e.g. Wong et al., 2011), potentially complicating the paleo-hydrological interpretation of stalagmitic Mg records. In addition, these records may be influenced by changes in temperature, which determines the distribution of Mg into calcite (DMg), possible kinetic effects during rapid precipitation (Rimstidt et al., 1998), or variable Mg input in detrital particles (Belli et al., 2017) or marine aerosols (Baldini et al., 2015).

In some stalagmitic records, Mg and $\delta^{13}C$ are positively correlated (e.g. Johnson et al., 2006), a relationship potentially helpful to understand the controls on $\delta^{13}C$ variation in such cases. Stalagmitic $\delta^{13}C$ mainly depends on the balance of two carbon sources in dripwater: relatively light, soil-derived CO_2, and isotopically heavier carbonate from dissolved hostrock. Their relative proportions depend on the degree of open-versus closed-system dissolution (Fohlmeister et al., 2011; Fairchild and Baker, 2012). Therefore, higher stalagmitic $\delta^{13}C$ values can result from increasing the contribution of hostrock-derived carbon, linked to increased water-rock interaction during drier periods (Bajo et al., 2017). This effect should also increase dripwater Mg/Ca ratios, providing a plausible explanation for the $\delta^{13}C$-Mg covariation trends in stalagmites. Also, and similar to the case of Mg, both dripwater and stalagmitic $\delta^{13}C$

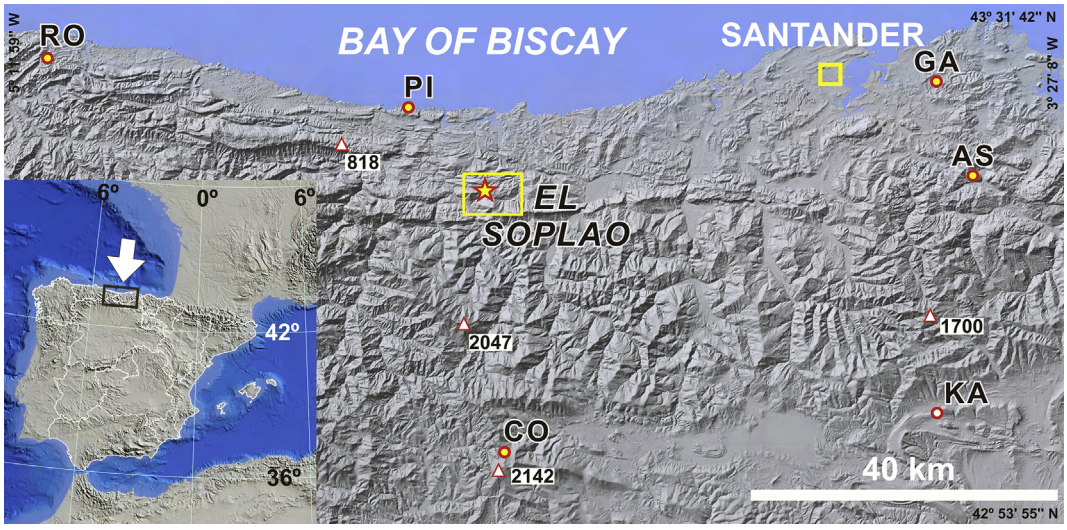

Fig. 1. Location of El Soplao cave in the Cantabrian Cordillera (N Spain), including elevations (m a.s.l) of representative peaks (triangles) and other caves mentioned in the text: Cobre (CO), Kaite (KA), Asiul (AS), La Garma (GA), El Pindal (PI) and Rosa (RO).

tend to increase during periods of enhanced PCP due to the associated degassing (Mickler et al., 2004; Frisia et al., 2011). This provides an additional explanation for the δ^{13}C-Mg covariation trends, regardless of the causes of the PCP enhancements: decreased drip rates during drier periods (Johnson et al., 2006) or enhanced ventilation (Spötl et al., 2005; Frisia et al., 2011; Johnston et al., 2013).

Here, we evaluate the paleohydrological significance of stalagmitic δ^{13}C-Mg covariation trends partly based on previously published data from modern dripwaters and the corresponding stalagmitic calcites from this cave, which both show high and variable Mg/Ca ratios controlled by PCP and subordinately by water-rock interaction (Rossi and Lozano, 2016). In addition, the cave hosting the studied speleothem is particularly suitable for using Mg as a paleohydrological proxy: the high background Mg contents facilitate not only obtaining high resolution Mg records (e.g. by using an electron microprobe) but also their interpretation, by limiting the relative importance of other possible Mg sources apart from dissolved dolomitic hostrock (such as detrital particles or aerosols).

2. Cave setting

The El Soplao-Torca-Ancha-Juñoso cave system is located in the Arnero Sierra, N Spain, ~12 km from the coastline (Fig. 1). With a maximum elevation of 683 m, this E-W-trending sierra (suppl. Fig. S1) lies in the Northern watershed of the Cantabrian Cordillera. Nearby, the highest elevations are in the Picos de Europa- and Peña-Sagra Sierra massifs, which may reach ~2600 and ~2000 m a.s.l., respectively, and were glaciated during the late Pleistocene. Current climate is temperate and wet (mean annual rainfall exceeding 1200 mm), with a dominant Atlantic influence (Ancell and Célis, 2013). Near the main cave entrance (550 m a.s.l.), mean annual temperature is 11.3 °C (data from El Soplao weather station).

The cave system (~23 km of surveyed passages; elevation range: ~350–575 m a.s.l.) is developed in steeply dipping Aptian dolostones sandwiched between Aptian limestones (Fig. 2A). Apart from abundant fractures of typically sub-millimeter-scale aperture, the dolostone contains intraparticle, intercrystalline, vuggy, and breccia porosity, contrasting with the negligible matrix porosity of the limestones (Rossi et al., 2017). Due to the dip of the strata (~40° to the N), the terrain above the cave mainly consists of limestone outcrops (Fig. 2A). However, because preferential flow is down the dip of the strata, the catchment areas of cave dripwaters are mainly dolostone outcrops. To the west, these outcrops are manly covered by shrubs/grasses, whereas to the east they contain beech forest (Fig. 2A).

Stalagmite SIR-1 (550 mm tall) grew in a sub-horizontal passage (SIR: 43° 17′ 46.23″N, 4° 23′ 37.21″W, 490 m a.s.l; Fig. 2B), ~120 m below the land surface. This passage is a segment of a ~2-km-long low-gradient relict canyon partially filled by siliciclastic sediments and unique ferromanganese speleo-stromatolites formed at the water table during the Early Pleistocene (Rossi et al., 2010). U-series dating indicates discontinuous growth of aragonite and calcite speleothems in the canyon for the last ~1.5 Ma (Rossi et al., 2016). The catchment area of SIR dripwaters mainly consists of rugged dolostone outcrops with shrubby vegetation (Fig. 2C). SIR-1 was inactive when sampled. It was fed by a 25-cm-long, thickening-downwards, bulbous stalactite located ~1.3 m above the stalagmite. Twelve U-Th dates from SIR-1 were obtained by Rossi et al. (2016) to constrain the minimum age of the stromatolitic and siliciclastic deposits. These dates revealed a prominent hiatus in SIR-1 (Hiatus-1) separating an Upper Pleistocene interval (from 78.9 to 33.5 ka) from a Lateglacial to Early Holocene section (from 14.5 to 8.1 ka). In the present study, we use the previously published dates from the post-Hiatus-1 section, along with 11 new U-Th dates from this section, referring the depths of both sets of dates to a new composite transect (section 3.3).

SIR passage contains abundant calcitic stalactites and stalagmites (Fig. 2C; Suppl. Fig. S2), some of which are currently active. Relative humidity (RH) is close to saturation and air temperature is 10.8 °C ±0.2 (Rossi and Lozano, 2016). The high thermal stability of SIR is related to its location, midway between the cave entrances that drive summer and winter air into the cave (Rossi and Lozano, 2016). Therefore SIR temperature is not significantly biased to summer or winter values, likely approaching the mean air annual temperature of the terrain above the cave. Air CO_2 typically ranges ~450–650 ppmv, with minimum CO_2 values occurring when cave-air circulation is in winter mode (i.e. typically from November to March) (Rossi and Lozano, 2016).

SIR dripwaters have lower supersaturations (mean calcite Saturation Index, $SI_{CALCITE}$: 0.39 ± 0.07) compared to average values for calcite-precipitating drips elsewhere in the cave (0.71 ± 0.22) (Rossi and Lozano, 2016). Similar to other sites in the cave, the Mg/Ca ratios of stalagmite-feeding SIR dripwaters show relatively minor seasonal variation but change notably from drip to drip (0.50–0.73 mol/mol) and are inversely correlated to drip discharge (Suppl. Fig. S4), implying that drip rate is a major control on the Mg/Ca ratios of dripwater and thus on the Mg content of the corresponding calcites (Rossi and Lozano, 2016). Given that long-term variations in drip discharge should be mainly controlled by rainfall, stalagmitic [Mg] records from this cave have a great potential as paleohydrological proxy.

3. Methods

3.1. Stalagmite slabbing and thin sectioning

A 1.5 cm-thick axial slab were cut from SIR-1 with a diamond saw, grinded and polished with resin-bonded diamond discs, and scanned (Fig. 3A). 22 blocks, each 4 cm by 2.5 cm, were cut from the slab using a 300 μm-thick diamond blade to minimize the loss of material. The surfaces of the blocks were vacuum-impregnated with blue-died epoxy to highlight porosity and to minimize abrasive penetration into pores. Double-polished thin sections were cut from the blocks using a 400 μm-thick diamond blade, so that the thin sections and the surfaces of the remaining blocks are virtually equivalent.

3.2. Fluorescence imaging and lamina counting

Fluorescence (FL) images were obtained under violet-blue light excitation using an Olympus BX-61 microscope equipped with mercury-vapor epi-illumination. For each thin section, ~21 12.5-megapixel images were combined with photoshop, forming a mosaic covering the entire thin-section. Unless stated otherwise, distances along the growth axis are expressed as depths from the stalagmite top. Between 0 and 285 mm of depth, fluorescing laminae were counted on the images. To facilitate counting, reference markers were labeled every ~20 to ~30 laminae. Counts between two successive markers were repeated in at least two different transects, and the resultant uncertainties (plus/minus a number of laminae) assigned to the corresponding interval. Depths below the stalagmite top were recorded for each lamina (precision: ±0.01 mm). Considering the annual duration of the laminae (section 5.1), a high-resolution growth-rate record was derived from the recorded depths at 10-year increments. An additional, long-term growth rate record was derived from the age-depth model (section 4.2), at steps matching significant changes in the lamina-counting-derived growth-rate (i.e. at depths of ~6, 24, 42, 147,

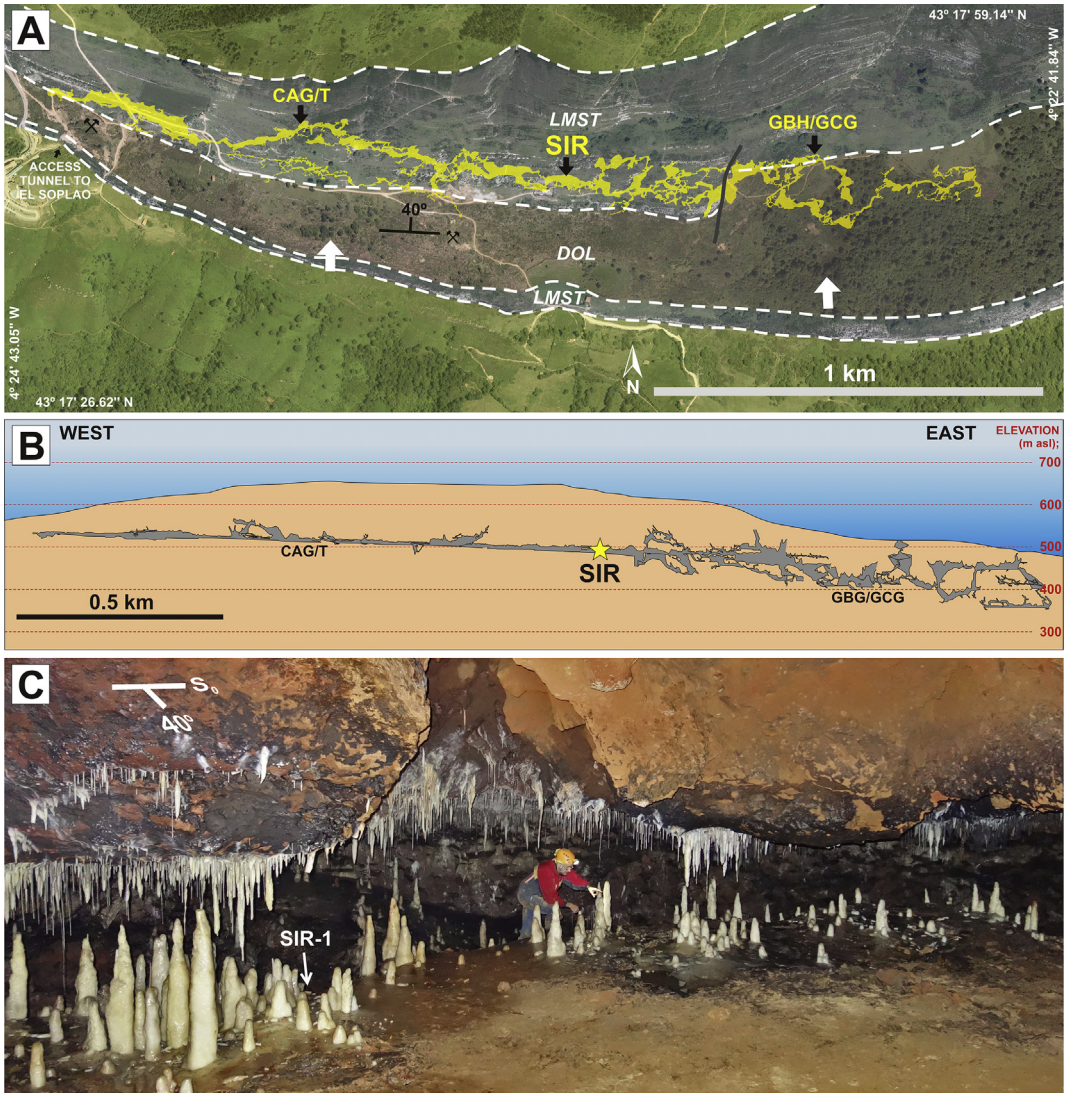

Fig. 2. A: Plan view of the cave superimposed on aerial images and the corresponding geological map (LMST: limestone; DOL: dolostone). Black arrows point to relevant dripsites in the cave (CAG/T, SIR, and GBG/GCG: Rossi and Lozano, 2016). White arrows indicate recharge areas having forest or forest patches. B: E-W projected view of the cave system and the land surface, showing the SIR site. C: General view of the SIR site.

232, 256, 277, and 281 mm) or the locations of U-Th dates (below 285 mm of depth). The thin sections were also examined under cross-polarized and reflected light to determine crystal fabrics and possible detrital layers.

3.3. U-Th dating

11 new samples for U-Th dating were obtained using a hand-held drill with a 0.8-mm-diameter diamond tip, following visible laminae. The locations of theses dates, and those published by Rossi et al. (2016), are shown in Fig. 3 and expressed in Table 1 as depths along the transect used to obtain the trace-element and stable isotopic data (section 3.4). The samples (~20-mg each) were drilled in the same blocks used to cut the thin sections, following ultrasonic cleaning. Activity ratios were determined using a Nu Instruments multicollector inductively coupled plasma mass spectrometer at the University of Melbourne following the procedures of Hellstrom (2003). U-Th ages were calculated using the decay constants of Cheng et al. (2013). An initial $^{230}Th/^{232}Th$ ratio of 1.5 ± 1.5 was assumed to calculate corrected ages (Hellstrom, 2006). In most samples, measured $^{230}Th/^{232}Th$ activity ratios are relatively large (i.e. above ~300), therefore the corrections accounting for initial (detrital) ^{230}Th are insignificant. Five subsamples had significant detrital Th, requiring age corrections ranging from 0.2 to 2.5 ka. The initial $^{234}U/^{238}U$ activity ratio was calculated from the measured $^{234}U/^{238}U$ activity ratio and the Th-corrected ages. 95% uncertainties were propagated by Monte-Carlo simulation. One date (at 254.35 mm) was discarded due to analytical problems. After unsuccessful attempts of bringing three discordant dates into correct stratigraphic order by changing the assumed initial $^{230}Th/^{232}Th$ ratio, these dates were considered outliers and discarded from the age-depth model, which was generated using the corrected U-Th ages.

3.4. Electron microprobe measurements

Electron MicroProbe (EMP) measurements were performed on graphite-coated polished thin sections using a JEOL JXA-8900 superprobe, along a composite transect that roughly followed the maximum extension axis. We used the FL images (section 3.2) to

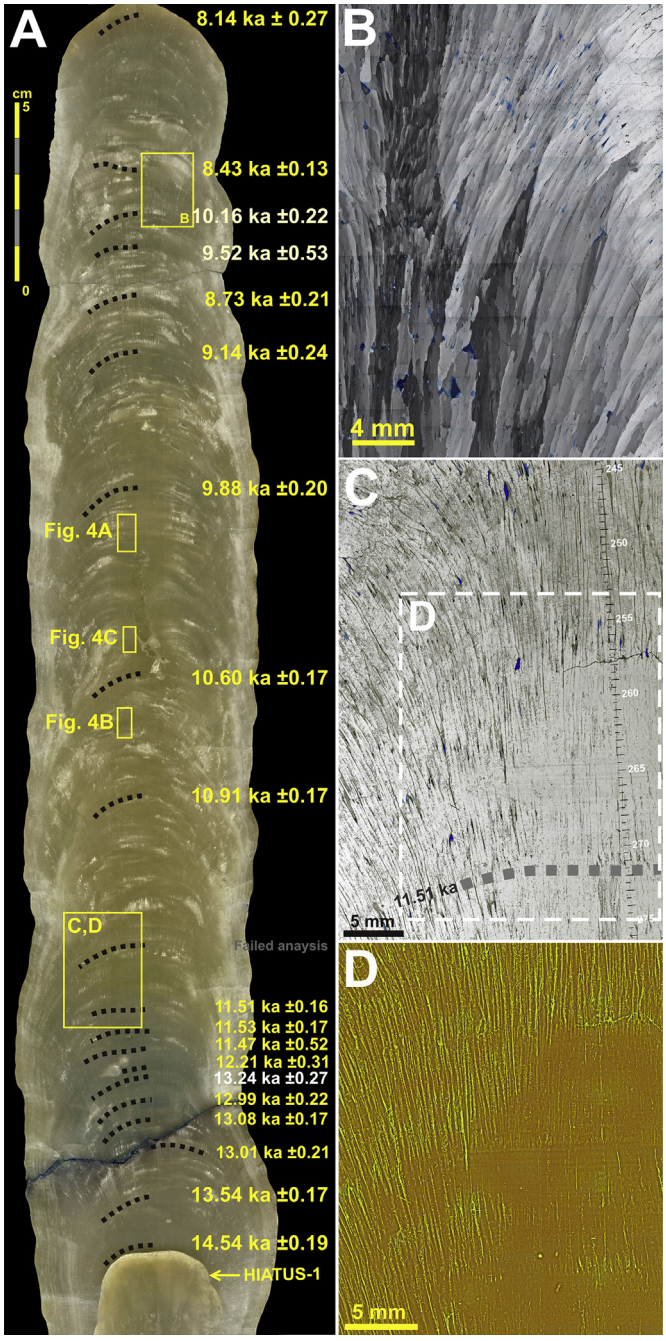

Fig. 3. A: Polished slab 1 of SIR-1, showing the locations of U-Th subsamples (Table 1). Samples in white text were defined as outliers (see text and Table 1). B: Transmitted-light image (semicrossed nicols) showing the elongated-columnar fabric. C–D: Transmitted-light (C) and FL (D) images illustrating the texture change from columnar compact to open columnar calcite at ~260 mm (section 4.1). Depths are in mm.

plan transects, avoiding pores as much as possible and minimizing gaps between thin sections. Both spot and line EMP measurements were performed.

For the spot analyses, the probe operated at 15 kV, 10 nA, 5 μm beam diameter, and 200 μm spacing between spots. Following our age-depth model, for the Early Holocene this typically translates into one analysis every ~2.5 years, each analysis represented the calcite precipitated in ~3 weeks. Mean detection limits are 167 μg/g for Mg, 201 μg/g for Ca, 225 μg/g for Sr, 592 μg/g for Zn and 206 μg/g for S. The standards used were calcite (Ca), dolomite (Mg), strontianite (Sr), gahnite (Zn), and galena (S). For Mg, a TAPH diffracting crystal and counting times of 30 s (peak) and 30 s (background) were used. After adding to the measured cations the amounts of CO_3 required by stoichiometry, totals between 97 and 103% were accepted.

For the line analyses, the probe operated at 20 kV, 150 nA, 5 μm beam diameter, 10 μm spacing between spots, and 1 s dwell time. According to our age model, in the Early Holocene this translates into one analysis centered every ~1.5 months, each analysis representing ~3 weeks of calcite precipitation. The quality of individual analyses was monitored using the TOPO and Ca signals, allowing the removal of bad analyses in holes or dust. To further check quality and consistency, in each thin section we measured the counts of Mg and Ca in two parallel transects spaced 100 μm apart (one for Mg-Ca-P-Sr-Zn and the other for Mg-Ca-Si-Al-K). With the exception of possible bad analyses, the Mg signal was regularly virtually identical in the two parallel transects, indicating that overlooked micropores have not significantly influenced the records. Of the two transects, the one with the least number of bad analyses was selected to build a composite Mg transect of the stalagmite. Mg counts were converted to %Mg by linear regression with the corresponding spot analyses ($R^2 = 0.96$), which seems reasonable as Mg is the only trace element that shows significant variation at EMP scale. The resulting record defines the same trends as the spot-based profile but with much higher resolution (Suppl. Fig. S3A), supporting the consistency of the Mg records. In intervals with well developed FL lamination (section 4.1), additional EMP lines were obtained with higher resolution (0-μm beam diameter, 1-μm spacing between spots), using 20 kV, 30 nA, and 1 s dwell time.

Locally, oscillations in the Mg-count signal suggest the influence of noise. However, the higher resolution (1-μm) Mg profiles show that most of these oscillations can be explained by intra-annual variations (section 4.3). Regarding the spot-based profiles, their noisier aspect (Suppl. Fig. S3A) is related to their inferior spatial resolution, and likely to random capturing of seasonal variations (section 4.3). Therefore, the spot-based profiles were only used for calibration purposes.

3.5. Stable isotope analyses

$\delta^{13}C$ and $\delta^{18}O$ sub-samples were drilled from the blocks used to cut the thin sections, following the EMP transect at 1-mm increments, using a 0.8-mm-diameter drill tip. On average, each subsample represents 11 years in the Early Holocene and 38 years in the Lateglacial. After drilling the subsamples, the blocks were scanned and the resulting images superimposed on the corresponding FL images, locating the stable-isotope holes in the EMP transects. The $\delta^{13}C$ and $\delta^{18}O$ analyses were performed at the Stable Isotope Laboratory of the University of Michigan. The samples were roasted in vacuo for one hour at 200 °C and subsequently reacted with anhydrous phosphoric acid at 77 °C in a Finnigan MAT Kiel IV preparation device coupled to the inlet of a Finnigan MAT 251 triple-collector isotope ratio mass spectrometer. O-17 corrected data were corrected for acid fractionation and source mixing by calibration to a best-fit regression line defined by standards NBS 18 and NBS 19. Values are reported as ‰ deviations relative to V-PDB. Measured precision is better than 0.1‰ for both $\delta^{13}C$ and $\delta^{18}O$.

4. Results

4.1. Calcite texture and fluorescence

SIR-1 is formed by radiating palisades of columnar crystals with length-to-width ratios exceeding 6:1 (elongated columnar fabric:

Table 1
Uranium-series analyses (brackets denote activity ratios). Activity ratios were determined after Hellstrom (2003). Age in ka before present is corrected for initial ^{230}Th using equation (1) of Hellstrom (2006), the decay constants of Cheng et al. (2013) and [^{230}Th/^{232}Th]i of 1.5 ± 1.5. Initial [^{234}U/^{238}U] is calculated using the corrected age. Ages refer to the date of analysis (2016). All uncertainties are two-sigma.

Depth Mm		[^{230}Th/^{238}U]	±95%	[^{234}U/^{238}U]	±95%	[^{232}Th/^{238}U]	±95%	[^{230}Th/^{232}Th]	U-Th age ka	±95%	[^{234}U/^{238}U] Initial	±95%
5	†	0.0987	0.0025	1.3443	0.0061	0.001266	0.000036	78.0	8.14	0.27	1.352	0.006
46		0.1012	0.0010	1.3424	0.0054	0.000762	0.000008	132.8	8.43	0.13	1.351	0.005
59	*†	0.1193	0.0023	1.3287	0.0041	0.000506	0.000010	235.9	10.16	0.22	1.338	0.004
67	*	0.1179	0.0015	1.3371	0.0081	0.004150	0.000012	28.4 9	52	0.53	1.346	0.008
80		0.1041	0.0020	1.3317	0.0060	0.000931	0.000012	111.8	8.73	0.21	1.340	0.006
95		0.1091	0.0020	1.3314	0.0069	0.001232	0.000014	88.6 9	14	0.24	1.340	0.007
132	†	0.1174	0.0022	1.3459	0.0049	0.000246	0.000010	477.5	9.88	0.20	1.356	0.005
182	†	0.1256	0.0018	1.3454	0.0057	0.000383	0.000015	328.3	10.60	0.17	1.356	0.006
215	†	0.1274	0.0018	1.3307	0.0037	0.000179	0.000029	711.0	10.91	0.17	1.341	0.004
272		0.1370	0.0014	1.3526	0.0076	0.000680	0.000003	201.4	11.51	0.16	1.364	0.008
277		0.1388	0.0017	1.3687	0.0059	0.000638	0.000011	217.7	11.53	0.17	1.381	0.006
283		0.1423	0.0015	1.3619	0.0029	0.004237	0.000013	33.6	11.47	0.52	1.374	0.003
288		0.1489	0.0013	1.3678	0.0032	0.002440	0.000009	61.0	12.21	0.31	1.381	0.003
290	*†	0.1590	0.0029	1.3774	0.0067	0.000584	0.000009	272.2	13.24	0.27	1.392	0.007
296		0.1546	0.0021	1.3627	0.0080	0.000634	0.000005	243.9	12.99	0.22	1.376	0.008
302		0.1563	0.0016	1.3725	0.0079	0.000325	0.000002	480.5	13.08	0.17	1.387	0.008
308		0.1558	0.0021	1.3705	0.0062	0.000703	0.000011	221.6	13.01	0.21	1.384	0.006
332		0.1611	0.0015	1.3669	0.0078	0.000499	0.000018	322.7	13.54	0.17	1.381	0.008
335	†	0.1707	0.0020	1.3560	0.0040	0.000366	0.000006	466.8	14.54	0.19	1.371	0.004

*Outlier. †Published in Rossi et al. (2016).

Frisia, 2015) (Fig. 3B–C). Visible detrital material is absent, except for some faint layers in the ~2-mm-thick-interval above Hiatus-1. In the uppermost 252 mm, millimeter-scale pores are locally present (Fig. 3A). Fluorescent laminae regularly surround the pores, indicating that these represent primary growth features rather than products of dissolution. The shape of the apical stalagmitic growth surfaces is typically curved, except between ~260 and ~283 mm of depth where they are relatively flat (Fig. 3C–D). At ~297 mm of depth, the growth axis slightly shifted (Fig. 3B). Between 150 and 180 mm of depth, the growth surface developed a moderate apical depression (Fig. 3A).

Between ~7 and ~264 mm of depth, SIR-1 shows well-developed fluorescent laminae (Fig. 4), indicating that the corresponding calcite is largely unaffected by significant diagenetic recrystallization; otherwise the delicate FL laminae would have been obliterated of disrupted. This does not preclude subtler diagenetic alteration, as suggested by the localized presence (at 59 and 67 mm) of discordant U/Th ages (section 4.2). In the cross-sectioned stalagmite, the interval with well-defined FL laminae is yellowish (Fig. 3A). Below ~260 mm of depth, the definition of the FL laminae deteriorates, coincident with a textural change: columnar compact calcite with flat apical growth surfaces (below) to open columnar calcite (sensu Frisia, 2015) with curved apical growth surfaces (above) (Fig. 3C–D).

FL Lamination is defined by regularly spaced, thin (<~10 μm), highly fluorescing bands separating thicker, less fluorescent intervals. Each pair formed by a thin fluorescing hairline and a non-fluorescing band is considered here as one lamina. Above 7 mm and below 264 mm of depth, the FL laminae are fainter and thinner. Below ~285 mm of depth, rhythmic FL laminae are absent. In the FL-laminated interval, lamina thickness typically ranges 50–110 μm, averaging 80 μm.

4.2. Age-depth model

U-Th dating (Table 1, Fig. 5A) indicates the studied record covers the Bølling-Allerød (B-A) interstadial, the YD, and the Early Holocene. The floating lamina chronology obtained in the upper 266.9 mm of depth was anchored to the U/Th age-depth model, by assigning to the youngest lamina the absolute age that minimizes the differences between the lamina chronology and the U-Th dates. The boundaries of the laminated interval are virtually coincident in both models, which agree within their error margins (Fig. 5B). Below 266.9 mm of depth, i.e. where both models intersect at 11.407 ka, the U-Th model is used. Above 266.9 mm of depth, the lamina-counting model is used. At this depth, the error of the U-Th model (±0.092 ka, 2σ) was assigned to the lamina-count model. Above 266.9 mm of depth, the uncertainty of the lamina-count model is increased progressively by accumulating the corresponding counting errors, at increments of ~20–30 laminae (section 3.2) (Fig. 5B). In the upper 266.9 mm of depth, using the lamina-count model (anchored to the U/Th model as explained above) is probably justified, given the significant anticorrelations observed between the rate of growth derived from lamina thickness and the corresponding [Mg] and δ^{13}C records (see section 4.3 below).

The U-Th outliers (section 3.4) are not linked to obvious petrographic alteration indications. Two outliers have [^{230}Th/^{232}Th] indicative of negligible detrital contamination. Therefore, their anomalously high calculated ages are probably linked to localized (at 59–67 mm) open system behavior (likely U-leaching), similar to Bajo et al. (2016). From 131.85 to 214.70 mm, 3 U-Th dates give slightly older ages than expected from lamina counts. Two U-Th dates (at 45.5 and 80.4 mm) are slightly younger than expected from lamina counts. These discrepancies could be related to minor and variable differences between the assumed initial [^{230}Th/^{232}Th] ratios and the actual ratios.

4.3. Mg-concentration, stable-isotope and growth-rate records

Mg concentrations (denoted [Mg]) mostly range from 0.3% to 0.8%, i.e. well above detection limits, and define consistent trends, showing the suitability of the EMP for obtaining highly spatially-resolved Mg data from this type of speleothem calcite. P, Sr, and Zn counts did not define clear trends and were considered noise. Similarly, most of the Si, Al, and K signals reflect background noise, with the exception of some localized peaks in the very first mm above Hiatus-1, corresponding to subtle detrital-bearing layers. In spot analyses, the concentrations of Sr, Zn and S were typically near or below detection limits; therefore they will not be considered

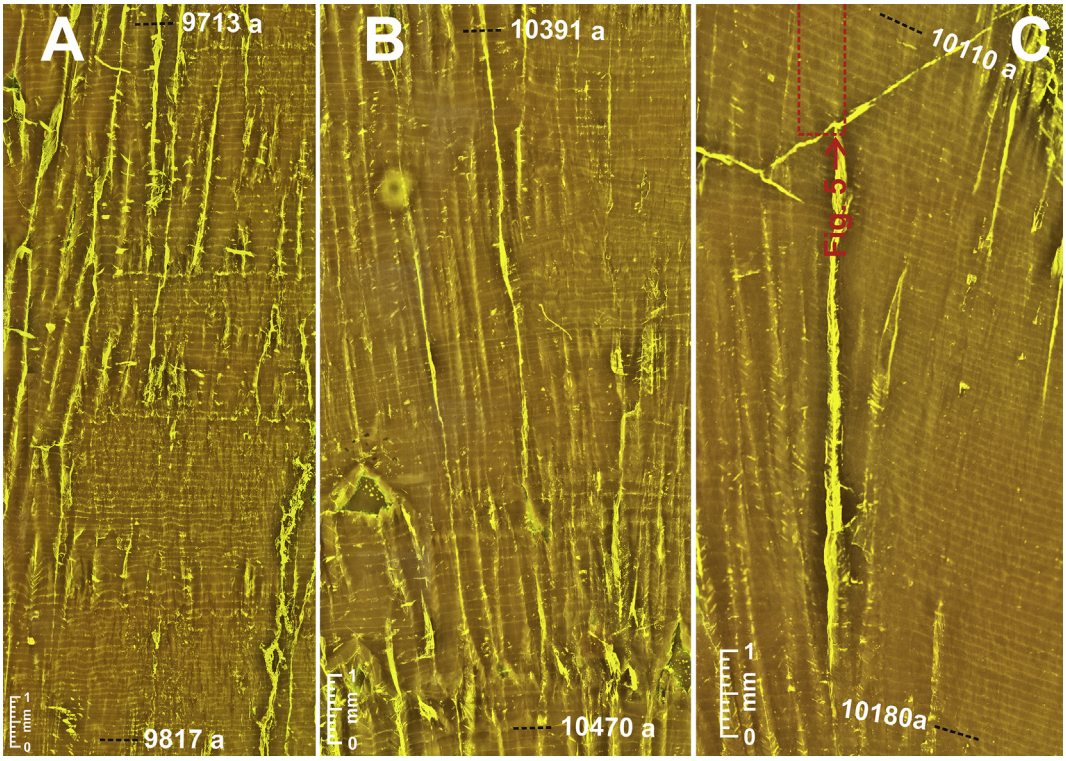

Fig. 4. Representative images of relatively well developed, annual (section 5.1), fluorescent laminae. The location of the images is shown in Fig. 3A.

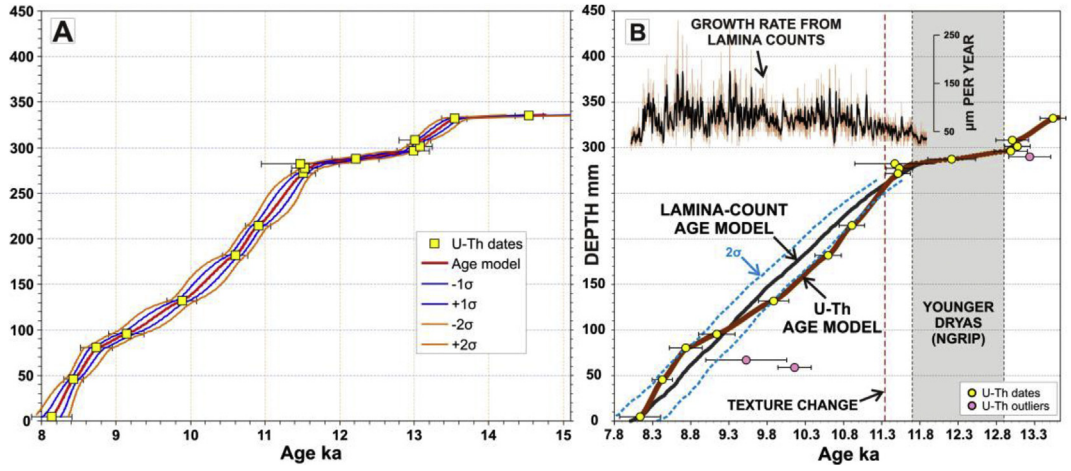

Fig. 5. A: U-Th model. B: Comparison of the U-Th model with the lamina-count-based model, showing the U-Th ages (error bars: 2σ). The black line represents the best fit of the floating lamina-counting chronology to the U-Th age model (section 4.2).

further. As revealed by the 1-µm-resolution line analyses in the FL-laminated intervals, [Mg] shows consistent intra-lamina variation, with Mg maxima typically occurring at or shortly after FL peaks (Fig. 6).

Fig. 7 and Suppl. Fig. S3B show the stable-isotope, [Mg] and growth-rate records. The corresponding data are available in Suppl. Table 1. $\delta^{13}C$, $\delta^{18}O$, [Mg], and initial $^{234}U/^{238}U$ ratios all show overall decreasing trends from the Lateglacial to the Holocene. In the youngest ~0.5 ka of the record, these proxies show moderate increasing trends, predating the growth cessation at ~8 ka. However, the most remarkable feature of the records is a prominent positive $\delta^{13}C$ excursion between ~280 and ~300 mm, whose chronology closely matches the YD as defined in Greenland ice (Fig. 7A). A notable $\delta^{18}O$ drop marks the YD onset, contrasting with the rather uniform $\delta^{18}O$ response at the YD-Holocene transition.

The [Mg] record describes several centennial-scale oscillations that tend to match those in the $\delta^{13}C$ record. Compared to the Lateglacial, the Early Holocene [Mg] record shows higher small-scale variability likely because its higher resolution allows capturing intra-annual variability (Fig. 6). Accordingly, the [Mg] record has been smoothed using 10-year (Early Holocene) and 5-year running averages (Lateglacial). In the Early Holocene, $\delta^{13}C$ and [Mg] are moderately but significantly correlated ($R^2 = 0.28$). In specific intervals, such covariation improves, particularly from 8.0 to 9.1 ka ($R^2 = 0.42$) and from 10.1 to 11.6 ka ($R^2 = 0.51$) (Suppl. Fig. S5). The [Mg]-$\delta^{13}C$ covariation changes at the YD-Early

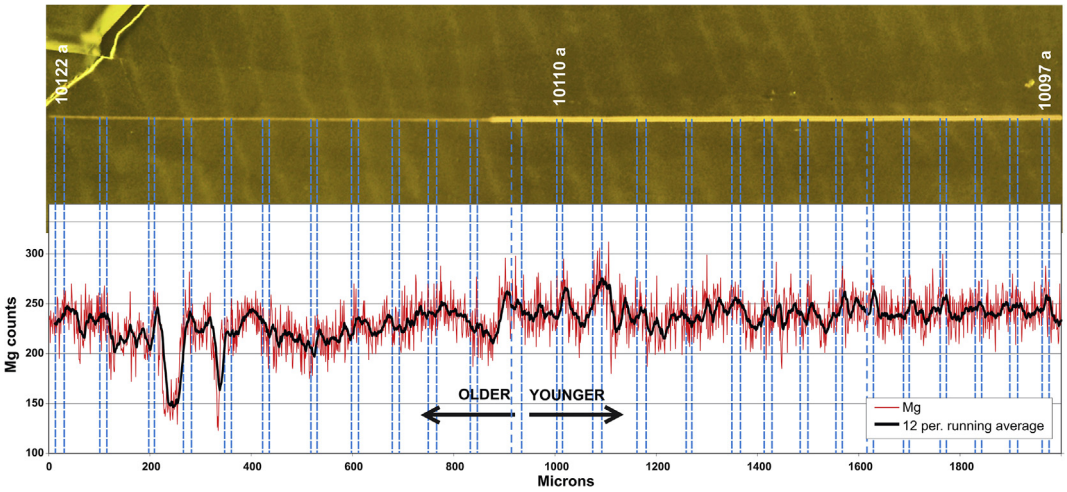

Fig. 6. High-resolution (data points every ~5 days) EMP transect across annual FL laminae, showing significant intra-annual [Mg] variations. Vertical lines mark the location of the brighter fluorescent bands that arguably formed during late fall-early winter (section 5.1).

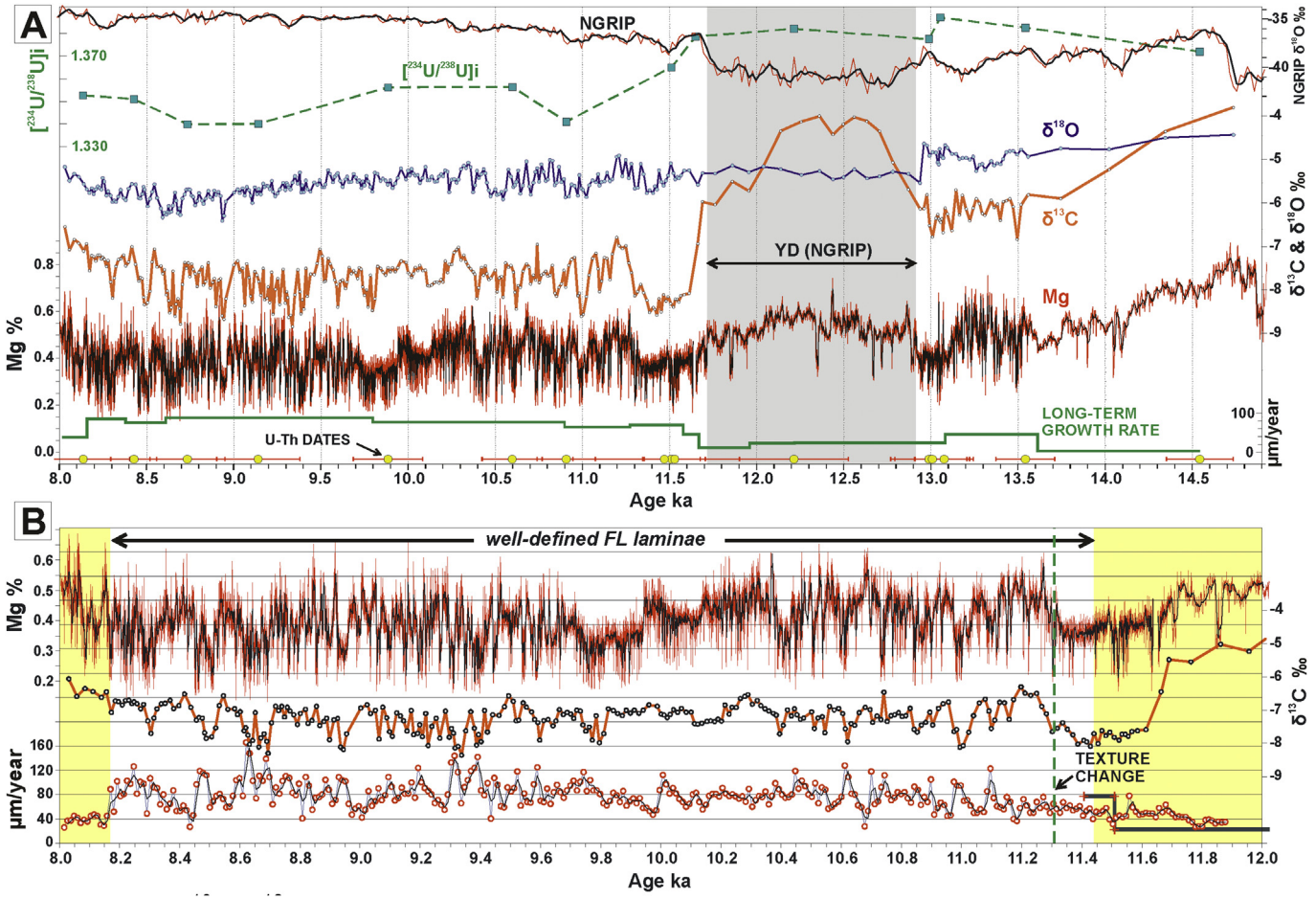

Fig. 7. A: $\delta^{13}C$, $\delta^{18}O$ ‰, and [Mg] data from SIR-1. The NGRIP record (Rasmussen et al., 2006) is included for comparison. B: Lamina-count-derived growth rate of SIR-1 compared to the corresponding [Mg] and $\delta^{13}C$ records to highlight their opposite behavior, indicating the interval showing well-defined FL laminae.

Holocene transition: in the Lateglacial, the cycles are longer and [Mg] values correspond to much higher $\delta^{13}C$ than in the Early Holocene.

Overall, growth rates are much higher during the Early Holocene than during the Lateglacial, and are particularly low during the YD (Fig. 7). Long-term growth rate (Fig. 7A) shows opposite behavior relative to $\delta^{13}C$ and [Mg], with periods of faster growth rate linked to lower [Mg] and $\delta^{13}C$. During the Early Holocene, short-term growth rate shows moderate but significant anticorrelations with both [Mg] ($R^2 = 0.18$) and $\delta^{13}C$ ($R^2 = 0.21$). In the younger part of the

Early Holocene, R^2 values increase to 0.32 ([Mg], 8–10 ka) and 0.30 ($\delta^{13}C$, 8–9.1 ka).

5. Discussion

5.1. Annual fluorescence banding

The Early Holocene FL laminae of SIR-1 are probably annual, as indicated by the good agreement in the duration of the laminated interval obtained from lamina counting and the U-Th age-depth model, within their respective uncertainties (Fig. 5B). Also, the FL laminae are highly regular and rhythmic (Figs. 4 and 6), strongly suggesting annual growth cycles, and very similar to those formed in comparable cave settings linked to flushing of soil organic matter during autumn rains (Tan et al., 2006; Baker et al., 2008). Currently in Cantabria, the first interval of intense rains after a moderate summer drought typically occurs during November–December. Therefore, assuming no drastic change in seasonal rain patterns during the Holocene, the bright FL lines of SIR-1 probably formed during late fall. Compared to other published records of stalagmitic FL laminae in the Cantabrian Cordillera (e.g. in Cobre cave: Rossi et al., 2014), the SIR-1 laminae are of relatively regular thickness and lack double or complex FL laminae. This is consistent with the relatively thick overburden (~120 m) above SIR-1 site, capable of mixing and homogenizing discrete rain events. However, the overburden was obviously not thick enough to erase the annual signals in FL (Fig. 4) and Mg (Fig. 6), pointing to a significant contribution of fracture flow in the vadose zone above SIR.

The Early Holocene, FL-laminated section of SIR-1 probably formed under a forested landscape. Currently, the surface above SIR is not forested and modern SIR stalagmitic calcites lack FL laminae or, when present, they are very poorly developed and limited to the highest-discharge drips (Rossi, unpublished data). By contrast, the Early Holocene section of SIR-1 shows an excellent development of FL laminae, arguably formed by seasonal flushing of soil organic matter. This suggests that vegetation conditions above SIR have changed significantly after the Early Holocene. Alternatively, the very poor development of FL laminae in modern SIR stalagmites could be linked to a hydrological change, as hydrology (e.g. drip rate) also influences the development of FL lamination (Genty et al., 1997; Baker et al., 2008). However, in modern SIR stalagmites FL lamination is poorly developed even under high-discharge drips, pointing to a post-Early Holocene vegetation change. Given that well developed, annual FL lamination in stalagmites typically forms in caves located below forests (e.g. Genty et al., 1997; Frisia et al., 2003; Meyer et al., 2009; Dasgupta et al., 2010), the development of FL lamination in SIR-1 supports that the terrain above SIR was probably forested in the Early Holocene. The present-day patchy distribution of forest in the Arnero Sierra (Fig. 2a), including its removal above SIR site, could be linked to local climatic factors (such as the mid-Holocene drying event: Moreno et al., 2011) of simply to anthropic deforestation. Indeed, historical or pre-historical partial deforestation has likely occurred in the Sierra, either for cattle production (which continues today) or, more recently, for producing wood for roasting zinc ore from the local mines.

5.2. Origin of the variations in magnesium concentration

Kinetic effects, linked to rapid precipitation (e.g. Rimstidt et al., 1998), could have influenced the SIR-1 Mg record and thus need to be evaluated. In modern SIR calcites, such effects are unlikely given the relatively low supersaturations, high RH, the tested isotopic-equilibrium conditions and the elongated columnar crystal fabrics (Rossi and Lozano, 2016). These fabrics are virtually identical to those in SIR-1, indicating no major changes in supersaturation and arguing against significant kinetic effects influencing the Mg record. Regarding detrital Mg, in most of the studied section of SIR-1 its influence is probably insignificant, given: the low Si and Al contents (section 3.4); the large $^{230}Th/^{232}Th$ activity ratios (section 3.3); the apparent absence of visible detrital-rich bands (except near Hiatus-1); and especially the high background Mg contents imposed by the dolostone hostrock. Therefore, the notable Mg variations recorded by SIR-1 are most likely related to changes in the Mg/Ca ratio of precipitating waters and/or temperature.

Temperature-dependant variations in DMg could contribute to explain some of the observed Mg variations in SIR-1, as suggested by the different [Mg]-$\delta^{13}C$ relationships in the Lateglacial and Early Holocene intervals. In both sections, higher $\delta^{13}C$ correspond to higher [Mg]. However, comparable [Mg] values correspond to much higher $\delta^{13}C$ in the YD (Fig. 7A). Apart from possible vegetation changes influencing $\delta^{13}C$ (section 5.3), such behavior is consistent with reduced Mg incorporation into calcite during the YD linked to lower temperatures (DMg decreases with temperature). Indeed, cave temperatures were undoubtedly lower during the YD when regional temperatures dropped significantly as indicated by independent proxies (~4 °C in the sea surface: Naughton et al., 2016) (Fig. 8). Assuming a constant dripwater Mg/Ca and an Early Holocene cave temperature similar to present day, an increase of ~4 °C at the YD-Holocene transition would have increased SIR-1 [Mg] by about 900 ppm (Suppl. material). However, the actual change is not an increase, but a decrease of ~2400 ppm. Therefore temperature, which was undoubtedly a factor, was not the main control. Then, the main reason of the [Mg] decrease during the YD-Holocene transition was a major drop in dripwater Mg/Ca, probably from maximum values of ~1.1 mol/mol (YD) to values around ~0.5 (Suppl. material). In summary, at the YD-Early Holocene transition, the effect of temperature on DMg was superseded by a major change in dripwater Mg/Ca. However, the temperature effect contributes to explain why the [Mg]-$\delta^{13}C$ covariation changed across this transition.

From the above, it follows that the most plausible mechanism to explain the notable [Mg] variations recorded by SIR-1 is changing the Mg/Ca ratio of the precipitating dripwaters. This is also supported by the large intra-site and inter-site Mg/Ca variations of modern dripwaters, which are mainly controlled by PCP and water-rock interaction, respectively (Rossi and Lozano, 2016).

In a stalagmite from La Garma, located 60 km to the east of El Soplao, Baldini et al. (2015) reported a ~300 ppm increase in [Mg] during the YD-Holocene transition, i.e. the opposite to our observations in SIR-1 in which Mg decreased ~2400 ppm from the YD peak to the Earliest Holocene (Fig. 8). Since the temperature effect is insufficient to explain the observed increase in La Garma (Baldini et al., 2015), these authors assigned the relatively low [Mg] of the YD as mainly resulting from reduced input of marine aerosols linked to repositioning of westerly storm tracks. In El Soplao, calculations show that the contribution of marine-aerosol Mg to dripwater (such as in La Garma) is insignificant (Suppl. material), given the high background Mg contents. This is shown by the much higher Mg contents in El Soplao stalagmites (Rossi and Lozano, 2016) including SIR-1, compared to La Garma (Fig. 8).

Consequently, the main drivers of [Mg] changes in SIR-1 must be PCP and/or water-rock interaction. Both mechanisms are compatible with the [Mg]-$\delta^{13}C$ covariation trends observed in SIR-1. However, PCP was likely dominant, as suggested by (1) the bulbous shape of the corresponding stalactite, indicative of significant calcite precipitation prior to dripping; and (2) the moderate variability of the initial $^{234}U/^{238}U$ record (Fig. 7A), indicating no major changes in the degree of water-rock interaction during SIR-1 growth (section 5.3).

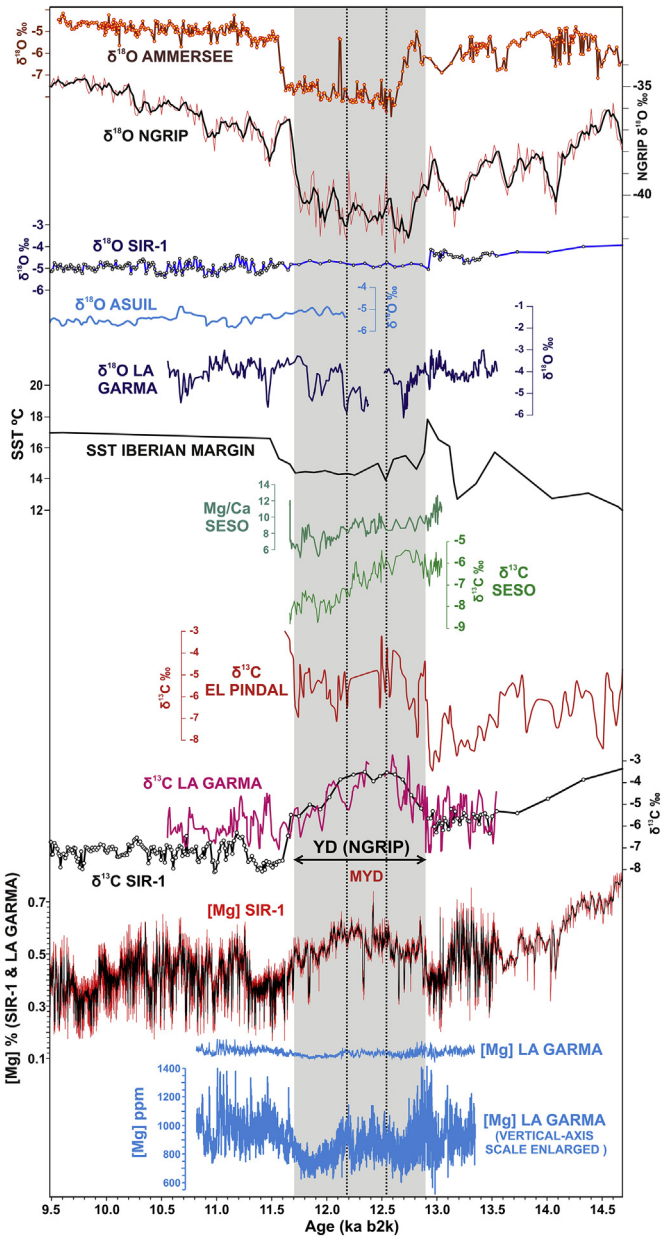

Fig. 8. Comparison of [Mg], $\delta^{13}C$ and $\delta^{18}O$ of SIR-1 to selected paleoclimate proxies from Cantabrian-Cordillera and Pyrenean stalagmites (El Pindal, La Garma, Asiul and Seso caves: Baldini et al., 2015, Smith et al., 2016a, Moreno et al., 2010, and Bartolomé et al., 2015, respectively), Iberian-margin cores (alkenone-based Sea Surface Temperature: Naughton et al., 2016), Greenland ice (NGRIP: Rasmussen et al., 2006) and Central European lacustrine sediments (Ammersee: von Grafenstein et al., 1999). MDY refers to the Mid YD transitional period. Note that the $\delta^{13}C$ and [Mg] records of La Garma and SIR-1 are plotted in common scales to highlight their similarities ($\delta^{13}C$) and differences (Mg), and the La Garma Mg record is also plotted using an enlarged vertical scale.

Most of the [Mg]-$\delta^{13}C$ covariation trends recorded by SIR-1 are probably not significantly influenced by changes in cave ventilation. Enhanced ventilation should lead to higher supersaturations (Spötl et al., 2005; Wong et al., 2011) and consequently to higher growth rates. However, both [Mg] and δ13C show opposite behavior relative to growth rate (section 4.3; Fig. 7), indicating that enhanced ventilation alone cannot explain the [Mg]-δ13C maxima. Therefore, discharge variations are probably the most feasible mechanism to produce much of the long-term PCP-related [Mg] variations recorded by SIR-1. This is consistent with the significant anticorrelations observed in individual drip sites of this cave (including SIR) between discharge and Mg/Ca (Rossi and Lozano, 2016). Furthermore, calculations based on the present-day DMg values determined in SIR by Rossi and Lozano (2016) show that the Early-Holocene [Mg] range of SIR-1 can be easily explained by discharge variations (Suppl. material).

The Early-Holocene intra-annual [Mg] cycles of SIR-1 (Fig. 6) probably respond to a combination of discharge variations and seasonal ventilation. [Mg] maxima typically match FL bands or occurred slightly after, implying the maxima mostly occurred during winter (section 5.1). Given the current thermal stability of SIR (section 2), it is unlikely that the intra-annual [Mg] cycles respond to temperature changes. Rather, most cycles are likely related to ventilation effects. This is consistent with the regularly higher supersaturations of present-day dripwaters during winter (Rossi and Lozano, 2016), which promote corresponding increases in dripwater Mg/Ca due to enhanced PCP. However, in some annual layers [Mg] maxima occur midway between FL bands, implying the maxima could have formed during summer. Since the Mg/Ca of modern dripwaters may increase during low-discharge events (Rossi and Lozano, 2016), such [Mg] maxima could be linked to occasional summer droughts.

5.3. Origin of $\delta^{13}C$ variability

Similar to other European stalagmite records (e.g. Genty et al., 2003), in SIR-1, higher $\delta^{13}C$ values are arguably linked to colder intervals with reduced soil productivity: $\delta^{13}C$ is remarkably higher during the Lateglacial compared to the Early Holocene, and is particularly high during the YD when regional temperatures dropped significantly (section 5.2). Also, SIR-1 growth rate is much reduced in periods of high $\delta^{13}C$. Given the strong temperature control on speleothem growth rates (Borsato et al., 2016), such relationship is consistent with reduced soil productivity during colder periods. This inference is also supported by the poor or null development of FL laminae (section 5.1) in the intervals of SIR-1 with higher $\delta^{13}C$ and lower growth rates.

Besides vegetation changes, drip-discharge variations can contribute to explain the $\delta^{13}C$ variability of SIR-1. This is suggested by the similar behaviors of the $\delta^{13}C$ and [Mg] records (Fig. 7), the latter of which is largely controlled by variable PCP linked to hydrological changes (section 5.2). In fact, speleothem $\delta^{13}C$ should increase in periods of enhanced PCP due to the preferential loss of light CO_2 during the associated degassing (Dreybrodt and Scholz, 2011). A PCP influence on the SIR-1 $\delta^{13}C$ record is also consistent with the observed intra-site covariation between $\delta^{13}C$ of modern calcites and the corresponding dripwater Mg/Ca (Rossi and Lozano, 2016), which is largely controlled by PCP. Apart from PCP, enhanced water-rock interaction could have contributed to increase the Lateglacial SIR-1 $\delta^{13}C$ values, as indicated by a corresponding moderate increase of initial $^{234}U/^{238}U$ values (Fig. 7A). Increases in this ratio typically reflect longer water residence time in the aquifer (Hellstrom and McCulloch, 2000), which may increase the contribution of isotopically heavier host-rock carbonate, increasing the $\delta^{13}C$ of dripwaters and precipitated calcite. However, this was probably a subordinate effect given that the initial $^{234}U/^{238}U$ activity ratios only increased by ~4% during the Lateglacial, remaining virtually constant during the BA and YD intervals.

In summary, regardless of the precise causes of the $\delta^{13}C$ increases in SIR-1 in periods with high [Mg] and low growth rates, such increases are linked to periods of colder (and drier) climate. This is particularly obvious for the prominent $\delta^{13}C$ positive excursion during the YD. A similar behavior has been observed in other southwestern European sites, where stalagmitic $\delta^{13}C$ is a good

marker of the vegetation and hydrology changes linked to the abrupt climatic oscillations of the last Glacial and Interglacial periods (Genty et al., 2006; Moreno et al., 2010; Baldini et al., 2015; Pérez-Mejías et al., 2017). In these and other comparable records, higher $\delta^{13}C$ values are commonly linked to increased Mg/Ca ratios (e.g. Rossi et al., 2014; Bartolomé et al., 2015; Pérez-Mejías et al., 2017), indicating that the colder intervals were associated with drier conditions.

In the Early Holocene section of SIR-1, the $\delta^{13}C$ values suggest that the vegetation cover above SIR could have changed compared to present-day: the mean Early-Holocene $\delta^{13}C$ values in SIR-1 (−7.25‰) are much lower than those of modern SIR stalagmitic calcites (average: −5.85‰: Rossi and Lozano, 2016), whose recharge area currently lacks forest (Fig. 2). However, the Early Holocene SIR-1 values are much closer to those of modern stalagmitic calcites from sites with forested recharge areas (GBH/GCG and CAG/T: Fig. 2A), which average −8.18‰ (Rossi and Lozano, 2016). This similitude further suggests that the area above SIR was forested during the Early Holocene, consistent with the good development of FL lamination in this interval (section 5.1). Still, Early-Holocene $\delta^{13}C$ values in SIR-1 are not identical to those of modern stalagmites formed under forest, likely because each drip site shows different degrees of water-rock interaction and PCP (Rossi and Lozano, 2016).

5.4. Interpretation of the $\delta^{18}O$ record

Given that speleothem $\delta^{18}O$ is controlled by a series of complex and competing factors, such as seasonal $\delta^{18}O$ changes of atmospheric precipitation, sources of water vapor, rainfall amount, surface and cave temperatures, or kinetic effects during $CaCO_3$ crystallization (Lachniet, 2009), our data are probably insufficient to determine with high confidence the main controls on SIR-1 $\delta^{18}O$. But still, some interpretations are possible.

In the studied cave, considerable homogenization of infiltrated rainwaters currently occur in the vadose zone, as indicated by the insignificant seasonal variations in $\delta^{18}O$ of individual drips and the narrow range of values throughout the cave (−6.65‰ ±0.18; N = 27: Rossi and Lozano, 2016). This is consistent with other studies in Cantabrian caves, which have revealed substantial homogenization of seasonal $\delta^{18}O$ signals in dripwaters (Comas-Bru and McDermott, 2015; Smith et al., 2016b). Assuming no major change in the vadose-zone configuration above SIR in the last ~15 ka, comparable homogenization of infiltrated rainwater $\delta^{18}O$ probably occurred during SIR-1 growth too.

SIR-1 probably precipitated near isotopic equilibrium, as suggested by the equilibrium or quasi-equilibrium precipitation conditions tested in modern stalagmitic calcites throughout the cave, including SIR site (Rossi and Lozano, 2016). In addition, columnar fabrics such as those of SIR-1 usually precipitate near isotopic equilibrium (Frisia et al., 2000), and from dripwaters with moderate and stable supersaturations ($SI_{CALCITE} < 0.5$) (Johnston et al., 2013). Indeed, modern SIR stalagmites precipitate from moderately supersaturated dripwater ($SI_{CALCITE}$: 0.39 ± 0.07) and also show columnar fabrics (Rossi and Lozano, 2016). However, deviations from isotopic equilibrium can occur in stalagmites with columnar fabric, especially with increasing cave temperature or decreasing drip rates (Johnston et al., 2013). In addition, extrapolating the present-day equilibrium precipitation conditions beyond the Holocene could be not justified, given the large vegetation and temperature changes involved at the YD-Early Holocene transition, as discussed above.

From the earliest Holocene to ~8.6 ka, SIR-1 $\delta^{18}O$ shows a general decreasing trend (from ten-period average values of −2‰ to −3.5‰, respectively: Fig. 7A), consistent with a corresponding increase in rainfall amount. In a coeval stalagmite from Asiul cave, located ~65 km to the east of El Soplao (Fig. 1), a similar trend was reported by Smith et al. (2016a) (Fig. 8). These authors interpreted the trend as reflecting a general increase in rainfall amounts during the Early Holocene, based on the present-day relationship between rainfall amount and rainwater $\delta^{18}O$ observed in Cantabria (Comas-Bru and McDermott, 2015; Smith et al., 2016b). The SIR-1 record supports such interpretation. In SIR-1, the increasing $\delta^{18}O$ trend reversed from ~8.5 to ~8.0 ka. Coevally, both [Mg] and $\delta^{13}C$ also tend to increase (Fig. 7B), indicating drier conditions. This further supports that the Early Holocene SIR-1 $\delta^{18}O$ variation mainly responds to variations in the amounts of precipitation.

Remarkably, SIR-1 shows almost no $\delta^{18}O$ change at the YD-Early Holocene transition, despite the large temperature and hydrology changes (section 5.2). Similarly, stalagmite ASR from the nearby Asiul cave does not show significant $\delta^{18}O$ change across that transition either (Smith et al., 2016a) (Fig. 8). Apparently, the various competing factors influencing speleothem $\delta^{18}O$ mutually cancelled during the transition. For instance, an increase in surface temperature tends to increase the $\delta^{18}O$ of rainfall, but the corresponding increase in cave temperature tends to decrease the $\delta^{18}O$ of speleothem calcite precipitated under isotopic equilibrium (Lachniet, 2009). However, other speleothem records from N Spain show $\delta^{18}O$ increases across the YD-Holocene transition, such in La Garma (Baldini et al., 2015) and particularly in Seso (Bartolomé et al., 2015).

The most remarkable feature of the SIR-1 $\delta^{18}O$ record is the abrupt ~0.9‰ negative shift marking the YD onset. The shift was not linked to the amount effect, which would have caused the opposite result since the YD was arguably dryer. The shift cannot be explained by kinetic effects linked to reduced drip rates, as such effect would increase $\delta^{18}O$. The shift is probably not a local effect, because other stalagmite records of the region also show coeval and comparable shifts (El Pindal: Moreno et al., 2010; La Garma: Baldini et al., 2015) (Fig. 8). In La Garma, the shift has been attributed to a marked drop in surface temperature that decreased rainfall $\delta^{18}O$ (Baldini et al., 2015) and surpassed the cave-temperature effect. However, the regional temperature change at the end of the YD was similar to the corresponding change at the YD onset (Naughton et al., 2016) (Fig. 8), and yet it induced no significant $\delta^{18}O$ change in SIR-1. This different behavior at the onset and end of the YD suggests that other effects apart from temperature could have contributed to lowering SIR-1 $\delta^{18}O$ at the YD onset.

At the YD onset, large volumes of low $\delta^{18}O$ glacial melt waters could have been released into the North Atlantic due to drainage of proglacial lakes (e.g., Muschitiello et al., 2015). Such hypothetical release would have lowered the $\delta^{18}O$ of sea surface waters and consequently of atmospheric precipitation in areas such as the Cantabrian Cordillera, potentially contributing to lowering SIR-1 $\delta^{18}O$ at that time. In fact, during the 8.2 ka event, other speleothems of the Cantabrian Cordillera show negative $\delta^{18}O$ shifts of comparable magnitude linked to freshwater releases into the N Atlantic (Domínguez-Villar et al., 2009). However, these shifts were relatively brief compared to the SIR-1 shift, which was rather permanent, suggesting different mechanisms. In addition, in La Garma the negative $\delta^{18}O$ shift recovered at the YD end (Baldini et al., 2015), contrasting with the SIR-1 behavior. Therefore, the influence of a possible freshwater release into the Atlantic on the SIR-1 $\delta^{18}O$ record remains hypothetical. Alternatively, the $\delta^{18}O$ shift could be related to a modification in the bulbous stalactite feeding SIR-1, coincident with the regional hydrology change, as suggested by the moderate coeval shift in growth axis at ~297 mm. However, our data is probably insufficient to evaluate this hypothesis. Therefore, the controls of the SIR-1 $\delta^{18}O$ behavior at the YD boundaries are uncertain.

5.5. Late Glacial-Early Holocene paleoclimate in the cantabrian region: constraints from SIR-1

5.5.1. Bølling-Allerød interstadial

Only two U-Th dates were obtained within this interval, in which the generally low growth rates induce increased dating uncertainty and decreased proxy-record resolution. Therefore, high-resolution paleoclimatic variability during this interval cannot be deduced with confidence. Overall, the SIR-1 B-A record reflects a warming and wetting trend, indicated by notable decreases in both $\delta^{13}C$ (by ~3‰), [Mg] (from ~0.8% to ~0.4%) and $\delta^{18}O$ (by ~0.5‰), and by a moderate increase in growth rate (from ~3 to ~45 μm/year) (Fig. 7). This trend agrees with the ocean and continental warming trends recorded in marine cores of the NW Iberian margin (Naughton et al., 2016) (Fig. 8) and stalagmites from other Cantabrian-Cordillera caves (Moreno et al., 2010). Still, the lack of FL laminae in the B-A section of SIR-1 suggests that soil productivity was poor, probably because the Arnero Sierra was still unforested.

5.5.2. Younger Dryas

In SIR-1, the YD is marked by a strong positive $\delta^{13}C$ excursion whose age (12.95 ± 0.14 ka to 11.62 ± 0.16) closely matches the YD chronology in the Greenland ice-core record (Rasmussen et al., 2006), in marine cores from the Iberian Margin (Naughton et al., 2016), and in other speleothem records from N Spain (Fig. 8), supporting the high synchronicity of the event in the N Atlantic region. The agreement of the $\delta^{13}C$ records from SIR-1 and La Garma (Baldini et al., 2015) is remarkable. In both cases the $\delta^{13}C$ values are very similar and describe virtually the same changes across the YD (Fig. 8), supporting that the $\delta^{13}C$ records are essentially reflecting regional changes and not local effects.

In SIR-1, the YD onset is clearly defined by notable increases in $\delta^{13}C$ and [Mg], and decreases in growth rate, indicating a transition to colder and drier climate as discussed above. However, in the Arnero Sierra the YD climate was not cold enough to completely stop SIR-1 growth, which continued albeit at slow rate. The corresponding cave (and land surface) temperature was probably not below ~6 °C (Suppl. material). This limit is consistent with the minimum temperature for significant speleothem growth observed in other comparable European mountain settings (~4.4 °C; Borsato et al., 2016). The altitude of the recharge area of El Soplao cave is about 600 m a.s.l. Therefore, the upper altitude limit for significant speleothem growth in the Cantabrian Cordillera was probably located around 900 m a.s.l. (assuming a surface air temperature gradient of 0.6 °C/100 m). To our knowledge, no speleothem records covering the YD have been published from Cantabrian-Cordillera caves located at altitudes above 600 m a.s.l. However, in the Pyrenees, which represent the eastern prolongation of the Cantabrian Cordillera, a speleothem record of the YD have been reported from a cave located at ~800 m a.s.l. (Bartolomé et al., 2015), supporting that the upper elevation limit of significant speleothem growth during the YD was probably located around ~900 m above present-day sea level.

The prominent $\delta^{13}C$ change recorded by SIR-1 during the YD is asymmetrical. The $\delta^{13}C$ increase at the YD onset was slower, possibly taking ~2 centuries to complete. This figure is relatively uncertain, given the intrinsic error of our age model and the absence of annual laminae in the corresponding interval. By contrast, the $\delta^{13}C$ decrease at the YD termination was faster, probably taking less than a century, as suggested by the number of FL laminae (~70, albeit poorly-defined) in the corresponding interval. A similar asymmetry is recorded in Greenland ice, where the cooling at the YD onset took more than two centuries while the concluding warming only lasted ~60 years (Steffensen et al., 2008) (Fig. 8), further supporting (1) the synchronicity of the event in Greenland and the Cantabrian Cordillera, and (2) the high sensitivity of SIR-1 $\delta^{13}C$ to changes in regional temperature.

Contrasting with the $\delta^{13}C$ behavior, SIR-1 [Mg] increases abruptly at the YD onset, showing a more gradual decline at the YD termination. Stalagmitic $\delta^{13}C$ is highly sensitive to changes in soil productivity, while [Mg] is particularly sensitive to hydrology (i.e. drip rate). Therefore, at the YD onset, the different responses of $\delta^{13}C$ and [Mg] suggest that the change in hydrology occurred faster than the associated vegetation/soil change. However, at the YD termination the vegetation/soil change was apparently faster than the hydrological change.

The SIR-1 [Mg] and $\delta^{13}C$ records support the division of the YD into two phases: an early YD, characterized by increasing $\delta^{13}C$ and [Mg] indicative of reduced soil productivity and increasing aridity; and a late YD showing the opposite trend (Fig. 8). A two-phase YD is also apparent in lacustrine records from central/northern Europe (Brauer et al., 2008; Bakke et al., 2009; Lane et al., 2013) and speleothem records from N Italy (Belli et al., 2017) and N Spain (Baldini et al., 2015; Bartolomé et al., 2015). The two YD phases have been interpreted as the result an overall northward migration of the westerly winds and associated atmospheric front systems, from central Europe (early YD) to N Europe (late YD) (Bakke et al., 2009). In those records, the transition between both phases is typically dated at ~12.1–12.2 ka, coincident with $\delta^{18}O$ excursions in other European speleothems (e.g. Genty et al., 2006) and lacustrine records (von Grafenstein et al., 1999, Fig. 8). However, the mid-YD transition was been shown to be diachronic, starting at 12.15 ka (b2k) in Norway, ~120 years earlier in Germany (Lane et al., 2013), an as early as 12.5 ka (b2k) in the Pyrenees (Seso cave: Bartolomé et al., 2015). In the Cantabrian speleothems (SIR-1; and GAR-01: Baldini et al., 2015), the Mg records apparently date the transition at ~12.2 ka, when both records start a clear decreasing trend (Fig. 8). However, if based on the SIR-1 $\delta^{13}C$ record, the transition apparently started earlier, as $\delta^{13}C$ shows a double peak at 12.5 and 12.3 ka, matching relatively high but variable [Mg] values in both SIR-1 and GAR-01 (Fig. 8). A somewhat comparable behavior is observed in Seso cave, where $\delta^{13}C$ starts declining at ~12.5 ka, while Mg/Ca begins a clear decreasing trend ~0.25 ka later (Bartolomé et al., 2015) (Fig. 8). Therefore, the speleothem records from El Soplao, La Garma (Baldini et al., 2015), and Seso (Bartolomé et al., 2015) are probably consistent with a relatively cold and dry, mid-YD transitional period that lasted about 3 centuries in N Spain (from ~12.5 to ~12.2 ka: Fig. 8).

The early YD is characterized in SIR-1 by indications of increasing aridity, similar to the trend recorded in a Central Pyrenean speleothem (Seso Cave; Bartolomé et al., 2015). However, in the nearby La Garma cave, the early YD [Mg] record is characterized by enhanced variability, interpreted as reflecting fluctuating wind strength and marine-aerosol input as the westerlies were positioned intermittently over Cantabria (Baldini et al., 2015). Interestingly, a similar association of cold and dry conditions with stronger westerly winds has been deduced for the early YD in central Europe (Brauer et al., 2008). During the late YD, both SIR-1 and GAR-01 [Mg] records show decreasing trends. For SIR-1, this trend reflects increasing moisture, whereas in La Garma the trend is probably linked to a coeval decrease in westerly wind strength, as the westerlies moved back towards the north (Baldini et al., 2015; Bartolomé et al., 2015).

5.5.3. Early Holocene

The earliest Holocene (~11.6–11.3 ka) is recorded in SIR-1 by relatively low and uniform [Mg] and $\delta^{13}C$, indicating humid climate. This is consistent with the findings of Morellón et al. (2018), who inferred a quasi-immediate increase in humidity in NW Iberia at the YD-Holocene transition, based on the fast recovery of lake

levels. In the oldest part of the ~11.6–11.3-ka record of SIR-1, the modest growth rates and the poor development of FL laminae suggest that the landscape above the cave was still unforested. Well-defined FL annual lamination started at ~11.4 ka, suggesting the onset of forest vegetation. Therefore, the development of forest after the YD cold crisis probably took about two centuries.

From ~8.6 to ~11.3 ka, SIR-1 shows relatively high growth rates (~80–150 μm/year) and well developed annual lamination consistent with marked seasonality and forest vegetation. Coeval stalagmites from other Cantabrian-Cordillera caves also show high growth rates (Stoll et al., 2013; Smith et al., 2016a), in cases accompanied by annual lamination (Domínguez-Villar et al., 2009), indicating a relatively warm and humid regional climate. In SIR-1, the Early Holocene [Mg], $\delta^{13}C$, and growth-rate records show several centennial-scale cycles, whose analyses is beyond of the scope of this work. From ~9.7 to ~9.9 ka, [Mg] values are relatively low and uniform, i.e. similar to the Earliest Holocene, suggesting a relatively humid climate for that interval.

SIR-1 ceased growing at ~8.0 ka ±0.3, culminating a 0.5-ka trend of increasing aridity. Although the growth cessation could be accidental due to drip diversion or blockage, the preceding drying is probably climate-controlled. This is supported by the coeval (~8.0–8.4 ka) decrease in lamina thickness recorded by stalagmite LV5 from Kaite cave (located ~65 km to the SE of El Soplao: Fig. 1), indicating a corresponding reduction in rainfall (Domínguez-Villar et al., 2009). In LV5, the reduced growth rates occurred immediately after two prominent decadal $\delta^{18}O$ negative shifts (at ~8.40 and ~8.27 ka b2k) that represent the local response of the "8.2 ka" event (Domínguez-Villar et al., 2009). The SIR-1 $\delta^{18}O$ record does not capture these shifts, likely because its temporal resolution is not sufficiently high during the corresponding interval.

The temporary dryer conditions recorded by both SIR-1 and LV5 from ~8.5 to ~8.0 ka occurred within a ~3-ka period of optimum stalagmite-growth conditions in the region, identified in several coastal caves and lasting from ~9 to ~6 ka (Stoll et al., 2013). Still, and besides SIR-1, two stalagmites from El Pindal and Asiul caves stopped growth at around ~8.5–8.0 ka (7.8 ka ±0.4, Stoll et al., 2013; 8.6 ka ±0.4, Smith et al., 2016a), while other local stalagmites showed the opposite behavior, starting growing at around ~8.0 ka (Stoll et al., 2013; Smith et al., 2016a). This suggests that some hydrological re-organization could have occurred in the corresponding caves at ~8.5–8.0 ka, broadly coincident with the short-lived change to dryer conditions indicated in the high-resolution stalagmitic records of LV5 (Domínguez-Villar et al., 2009) and SIR-1 (this study).

6. Conclusions

As recorded by a Lateglacial to Early Holocene stalagmitic record from the Cantabrian Cordillera, colder intervals limited soil productivity and dripwater availability, leading to higher $\delta^{13}C$ and [Mg], reduced growth rate, and poor or null development of fluorescent lamination. Conversely, relatively warm and humid climates favored forest development and resulted in higher growth rates, lower $\delta^{13}C$ and [Mg], and well developed annual fluorescent lamination.

As recorded by SIR-1 and other stalagmites of the region, the YD is marked by a prominent positive $\delta^{13}C$ excursion whose chronology (12.95 ± 0.14 to 11.62 ± 0.16 ka) closely matches the YD as defined in Greenland ice, supporting a high YD synchronicity and the sensitivity of stalagmitic $\delta^{13}C$ in this region to changes in regional temperature.

Similar to Greenland, the prominent $\delta^{13}C$ change recorded by SIR-1 during the YD is asymmetrical, with a centennial-scale increase at the YD onset, and a faster (less than a century) decrease at the YD end. By contrast, SIR-1 [Mg] increases abruptly at the YD onset, showing a more gradual decline at the YD termination. At the YD onset, the different $\delta^{13}C$ and [Mg] responses suggest that the change in hydrology was faster than the associated vegetation/soil change. However, at the YD termination the vegetation/soil change was apparently faster than the hydrological change.

In SIR-1, the early YD record (until ~12.5 ka) is characterized by increasing $\delta^{13}C$ and [Mg] linked to increasing aridity, whereas the late YD (from ~12.2 ka on) shows the opposite trend. The transitional period separating both phases is characterized by a double $\delta^{13}C$ peak and relatively high and variable [Mg] values, reflecting relatively cold and dry conditions with moderate variability.

In the Arnero Sierra, mean annual YD temperatures were probably not below ~6 °C, allowing significant but relatively slow stalagmitic growth. The upper limit of significant speleothem growth In the Cantabrian Cordillera during the YD was probably located around ~900 m above present-day sea level.

At the YD-Holocene transition, the SIR-1 [Mg] record is influenced by temperature-dependant variations in the distribution of Mg into calcite. This effect was superseded by a major change in dripwater Mg/Ca linked to wetter conditions, from estimated maximum values of ~1.1 mol/mol (YD) to ~0.5 mol/mol (Earliest Holocene).

During most of the Early Holocene, the Arnero Sierra was forested and characterized by a relatively warm and humid seasonal climate. This climatic optimum is recorded in other stalagmitic records of the region, and is reflected in SIR-1 by well developed annual fluorescent lamination, higher growth rates, and overall decreasing $\delta^{18}O$. This latter trend is consistent with increasing rainfall amounts and is punctuated by centennial-scale oscillations. The intra-annual [Mg] cycles recorded by SIR-1 in the Early Holocene likely reflect a combination of seasonal ventilation effects and subordinately discharge variations. Similar to other high-resolution stalagmitic records of the Cordillera, from ~8.5 to 8.0 ka SIR-1 reflects a temporary drying trend.

Acknowledgments

Financial support was provided by grant ICT-Soplao-53.5.00.12.00 (IGME - Provincial Government of Cantabria - Turismo del Nansa). Alfredo Argumosa (El Soplao-SL) greatly facilitated our research in the cave. Jaime MacLennan provided data from El Soplao weather station. Alredo Fernández-Larios provided valuable EMP assistance and Lora Wingate kindly performed the stable isotope analyses. The highly constructive comments by Lisa Baldini, three anonymous QSR reviewers, and Editor Ana Moreno, greatly contributed to improve the manuscript.

Appendix A. Supplementary data

Supplementary data related to this article can be found at https://doi.org/10.1016/j.quascirev.2018.05.025.

References

Ancell, R., Célis, R., 2013. Termopluviometría de Cantabria durante el periodo 1981-2010. Agencia Estatal de Meteorología (AEMET), nota técnica n° 10. NIPO: 281-12-014-0; 20.

Bajo, P., Hellstrom, J., Frisia, S., Drysdale, R., Black, J., Woodhead, J., Borsato, A., Zanchetta, G., Wallace, M.W., Regattieri, E., Haese, R., 2016. "Cryptic" diagenesis and its implications for speleothem geochronologies. Quat. Sci. Rev. 148, 17–28.

Bajo, P., Borsato, A., Drysdale, R.N., Hua, Q., Frisia, S., Zanchetta, G., Hellstrom, J., Woodhead, J., 2017. Stalagmite carbon isotopes and dead carbon proportion (DCP) in a near-closed-system situation: an interplay between sulphuric and carbonic acid dissolution. Geochem. Cosmochim. Acta 210, 208–227.

Baker, A., Smith, C.L., Jex, C., Fairchild, I.J., Genty, D., Fuller, L., 2008. Annually laminated speleothems: a review. Int. J. Speleol. 37, 193–206.

Bakke, J., Lie, O., Heegaard, E., Dokken, T., Haug, G.H., Birks, H.H., Dulski, P., Nilsen, T.,

2009. Rapid oceanic and atmospheric changes during the Younger Dryas cold period. Nat. Geosci. 2, 202–205.
Baldini, L.M., McDermott, F., Baldini, J.U.L., Arias, P., Cueto, M., Fairchild, I.J., Hoffmann, D.L., Mattey, D.P., Müller, W., Nita, D.C., Ontañón, R., García-Moncó, C., Richards, D.A., 2015. Regional temperature, atmospheric circulation, and sea-ice variability within the Younger Dryas Event constrained using a speleothem from northern Iberia. Earth Planet Sci. Lett. 419, 101–110.
Bartolomé, M., Moreno, A., Sancho, C., Stoll, H.M., Cacho, I., Spötl, C., Belmonte, A., Edwards, R.L., Cheng, H., Hellstrom, J.C., 2015. Hydrological change in southern Europe responding to increasing North Atlantic overturning during Greenland stadial 1. Proc. Natl. Acad. Sci. Unit. States Am. 112, 6568–6572.
Belli, R., Frisia, S., Borsato, A., Drysdale, R., Hellstrom, J., Zhao, J.-x., Spötl, C., 2013. Regional climate variability and ecosystem responses to the last deglaciation in the northern hemisphere from stable isotope data and calcite fabrics in two northern Adriatic speleothems. Quat. Sci. Rev. 72, 146–158.
Belli, R., Borsato, A., Frisia, S., Drysdale, R., Maas, R., Greig, A., 2017. Investigating the hydrological significance of stalagmite geochemistry (Mg, Sr) using Sr isotope and particulate element records across the Late Glacial-to-Holocene transition. Geochem. Cosmochim. Acta 199, 247–263.
Borsato, A., Johnston, V.E., Frisia, S., Miorandi, R., Corradini, F., 2016. Temperature and altitudinal influence on karst dripwater chemistry: implications for regional-scale palaeoclimate reconstructions from speleothems. Geochem. Cosmochim. Acta 177, 275–297.
Brauer, A., Haug, G.H., Dulski, P., Sigman, D.M., Negendank, J.F.W., 2008. An abrupt wind shift in western Europe at the onset of the Younger Dryas cold period. Nat. Geosci. 1, 520–523.
Broecker, W.S., 1997. Thermohaline circulation, the Achilles Heel of our climate system: will man-made CO2 upset the current balance? Science 278, 1582–1588.
Broecker, W.S., Denton, G.H., Edwards, R.L., Cheng, H., Alley, R.B., Putnam, A.E., 2010. Putting the Younger Dryas cold event into context. Quat. Sci. Rev. 29, 1078–1081.
Cheng, H., Edwards, R.L., Shen, C.-C., Woodhead, J., Hellstrom, J., Wang, Y.J., Kong, X.G., Spötl, C., Wang, X.F., Alexander Jr., E.C., 2013. Improvements in 230Th dating, 230Th and 234U half-life values, and U-Th isotopic measurements by multi-collector inductively coupled plasma mass spectrometry. Earth Planet Sci. Lett. 371–372, 82–91.
Comas Bru, L., McDermott, F., 2015. Data-model comparison of soil-water δ-18O at a temperate site in N. Spain with implications for interpreting speleothem δ-18O. J. Hydrol. 530, 216–224.
Cruz, F., Burns, S., Jercinovic, M., Karmann, I., Sharp, W., Vuille, M., 2007. Evidence of rainfall variations in Southern Brazil from trace element ratios (Mg/Ca and Sr/Ca) in a Late Pliestocene stalagmite. Geochimimica et Cosmochimica Acta 71, 2250–2263.
Dasgupta, S., Saar, M.O., Edwards, R.L., Shen, C.-C., Cheng, H., Alexander, E.C., 2010. Three thousand years of extreme rainfall events recorded in stalagmites from Spring Valley Caverns, Minnesota. Earth Planet Sci. Lett. 300, 46–54.
De Deckker, P., Moros, M., Perner, K., Jansen, E., 2012. Influence of the tropics and southern westerlies on glacial interhemispheric asymmetry. Nat. Geosci. 5, 266–269.
Denton, G.H., Alley, R.B., Comer, G.C., Broecker, W.S., 2005. The role of seasonality in abrupt climate change. Quaternary Sciene Reviews 24, 1159–1182.
Domínguez-Villar, D., Fairchild, I.J., Baker, A., Wang, X., Edwards, R.L., Cheng, H., 2009. Oxygen Isotope Precipitation Anomaly in the North Atlantic Region during the 8.2 Ka Event: Geology, vol. 37, pp. 1095–1098.
Dreybrodt, W., Scholz, D., 2011. Climatic dependence of stable carbon and oxygen isotope signals recorded in speleothems: from soil water to speleothem calcite. Geochem. Cosmochim. Acta 75, 734–752.
Fairchild, I.J., Borsato, A., Tooth, A.F., Frisia, S., Hawkesworth, C.J., Huang, Y., McDermott, F., Spiro, B., 2000. Controls on trace element (Sr–Mg) compositions of carbonate cave waters: implications for speleothem climatic records. Chem. Geol. 166, 255–269.
Fairchild, I.J., Baker, A., 2012. Speleothem Science – from Process to Past Environments. Wiley-Blackwell, Chichester, 450 p.
Fohlmeister, J., Scholz, D., Kromer, B., Mangini, A., 2011. Modelling carbon isotopes of carbonates in cave drip water. Geochimimica et Cosmochimica Acta 75, 5219–5228.
Frisia, S., 2015. Microstratigraphic logging of calcite fabrics in speleothems as tool for palaeoclimate studies. Int. J. Speleol. 44, 1–16.
Frisia, S., Borsato, A., Fairchild, I.J., McDermott, F., 2000. Fabrics of speleothems from temperate-humid settings: growth mechanisms and environmental parameters. J. Sediment. Res. 70, 118321196.
Frisia, S., Borsato, A., Preto, N., McDermott, F., 2003. Late Holocene annual growth in three Alpine stalagmites records the influence of solar activity and the North Atlantic Oscillation on winter climate. Earth Planet Sci. Lett. 216, 411–424.
Frisia, S., Fairchild, I.J., Fohlmeister, J., Miorandi, R., Spötl, C., Borsato, A., 2011. Carbon mass-balance modelling and carbon isotope exchange processes in dynamic caves. Geochem. Cosmochim. Acta 75, 380–400.
Genty, D., Blamart, D., Ouahdi, R., Gilmour, M., Baker, A., Jouzel, J., Van-Exter, S., 2003. Precise dating of Dansgaard-Oeschger climatic oscillations in western Europe from stalagmite data. Nature 421, 833–837.
Genty, D., Blamart, D., Ghaleb, B., Plagnes, V., Causse, Ch, Bakalowicz, M., Zouari, K., Chkir, N., Hellstrom, J., Wainer, K., Bourges, F., 2006. Timing and dynamics of the last deglaciation from European and North Africa δ13C stalagmite profiles – comparison with Chinese and South Hemisphere stalagmites. Quat. Sci. Rev. 25, 2118–2142.
Genty, D., Baker, A., Barnes, W.L., 1997. Comparison of annual luminescent and visible laminae in stalagmites. Comptes Rendus Académie des Sciences Paris. Serie II 325, 193–200.
Hellstrom, J., 2003. Rapid and accurate U/Th dating using parallel ion-counting multi-collector ICP-MS. J. Anal. At. Spectrom. 18, 1346–1351.
Hellstrom, J., 2006. U–Th dating of speleothems with high initial 230Th using stratigraphical constraint. Quat. Geochronol. 1, 289–295.
Hellstrom, J.C., McCulloch, M.T., 2000. Multi-proxy constraints on the climatic significance of trace element records from a New Zealand speleothem. Earth Planet Sci. Lett. 179, 287–297.
Johnston, V.E., Borsato, A., Spötl, C., Frisia, S., Miorandi, R., 2013. Stable isotopes in caves over altitudinal gradients: fractionation behaviour and inferences for speleothem sensitivity to climate change. Clim. Past 9, 99–118.
Johnson, K., Hu, C., Belshaw, N., Henderson, G., 2006. Seasonal trace-element and stable-isotope variations in a Chinese speleothem: the potential for high-resolution paleomonsoon reconstruction. Earth Planet Sci. Lett. 244, 394–407.
Lachniet, M.S., 2009. Climatic and environmental controls on speleothem oxygen-isotope values. Quat. Sci. Rev. 28, 412–432.
Lane, C.S., Brauer, A., Blockley, S.P.E., Dulski, P., 2013. Volcanic ash reveals time-transgressive abrupt climate change during the Younger Dryas. Geology 41 (12), 1251–1254. https://doi.org/10.1130/G34867.1.
McDonald, J., Drysdale, R., Hill, D., Chisari, R., Wong, H., 2007. The hydrochemical response of cave drip waters to sub-annual and inter-annual climate variability, Wombeyan Caves, SE Australia. Chem. Geol. 244, 605–623.
Meyer, M.C., Cliff, R.A., Spötl, C., Knipping, M., Mangini, A., 2009. Speleothems from the earliest Quaternary: snapshots of paleoclimate and landscape evolution at the northern rim of the Alps. Quat. Sci. Rev. 28, 1374–1391.
Mickler, P.J., Banner, J.L., Stern, L., Asmerom, Y., Edwards, R.L., Ito, E., 2004. Stable isotope variations in modern tropical speleothems: evaluating equilibrium vs. kinetic isotope effects. Geochimimica et Cosmochimica Acta 68, 4381–4393.
Morellón, M., Aranbarri, J., Moreno, A., González-Sampériz, P., Valero-Garcés, B.L., 2018. Early Holocene humidity patterns in the Iberian Peninsula reconstructed from lake, pollen and speleothem records. Quat. Sci. Rev. 181, 1–18. https://doi.org/10.1016/j.quascirev.2017.11.016.
Moreno, A., López-Merino, L., Leira, M., Marco-Barba, J., González-Sampériz, P., Valero-Garcés, B., López-Sáez, J., Santos, L., Mata, P., Ito, E., 2011. Revealing the last 13,500 years of environmental history from the multiproxy record of a mountain lake (Lago Enol, northern Iberian Peninsula). J. Paleolimnol. 46, 327–349.
Moreno, A., Stoll, H., Jimenez-Sanchez, M., Cacho, I., Valero-Garces, B., Ito, E., Edwards, R.L., 2010. A speleothem record of glacial (25–11.6 kyr BP) rapid climatic changes from northern Iberian Peninsula. Global Planet. Change 71, 218–231.
Muñoz-García, M.B., Martín-Chivelet, J., Rossi, C., Ford, D., Schwarcz, H., 2007. Chronology of Termination II and the Last Interglacial Period in North Spain based on stable isotope records of stalagmites from Cueva del Cobre (Palencia). J. Iber. Geol. 33, 17–30.
Muschitiello, F., Pausata, F.S.R., Watson, J.E., Smittenberg, R.H., Salih, A.A.M., Brooks, S.J., Whitehouse, N.J., Karlatou-Charalampopoulou, A., Wohlfarth, B., 2015. Fennoscandian freshwater control on Greenland hydroclimate shifts at the onset of the Younger Dryas. Nat. Commun. 6, 8939.
Naughton, F., Sanchez Goñi, M.F., Rodrigues, T., Salgueiro, E., Costas, S., Desprat, S., Duprat, J., Michel, E., Rossignol, L., Zaragosi, S., Voelker, A.H.L., Abrantes, F., 2016. Climate variability across the last deglaciation in NW Iberia and its margin. Quat. Int. 414, 9–22.
Pérez-Mejías, C., Moreno, A., Sancho, C., Bartolomé, M., Stoll, H., Cacho, I., Cheng, H., Edwards, R.L., 2017. Abrupt climate changes during termination III in southern Europe. Proc. Natl. Acad. Sci. Unit. States Am. https://doi.org/10.1073/pnas.1619615114.
Rach, O., Brauer, A., Wilkes, H., Sachse, D., 2014. Delayed hydrological response to Greenland cooling at the onset of the Younger Dryas in western Europe. Nat. Geosci. 7, 109–112.
Railsback, L.B., Liang, F., Vidal-Romaní, J.R., Garrett, K.B., Sellers, R.C., Vaqueiro-Rodríguez, M., Grandal-d'Anglade, A., Cheng, H., Edwards, R.L., 2017. Radiometric, isotopic, and petrographic evidence of changing interglacials over the past 550,000 years from six stalagmites from the Serra do Courel in the Cordillera Cantábrica of northwestern Spain. Palaeogeography, Palaeoclimatology, Palaeoecology 466, 137–152.
Rasmussen, S.O., Andersen, K.K., Svensson, A.M., Steffensen, J.P., Vinther, B.M., Clausen, H.B., Siggaard-Andersen, M.-L., Johnsen, S.J., Larsen, L.B., Dahl-Jensen, D., Bigler, M., Röthlisberger, R., Fischer, H., Goto-Azuma, K., Hansson, M.E., Ruth, U., 2006. A new greenland ice core chronology for the last glacial termination. J. Geophys. Res. vol. 111. D06102.
Rimstidt, J.D., Balog, A., Webb, J., 1998. Distribution of trace elements between carbonate minerals and aqueous solutions. Geochem. Cosmochim. Acta 62, 1851–1863.
Rossi, C., Lozano, R.P., 2016. Hydrochemical controls on aragonite versus calcite precipitation in cave dripwaters. Geochem. Cosmochim. Acta 192, 70–96.
Rossi, C., Villalaín, J.J., Lozano, R.P., Hellstrom, J., 2016. Paleo-watertable definition using cave ferromanganese stromatolites and associated cave-wall notches (Sierra de Arnero, Spain). Geomorphology 261, 57–75.
Rossi, C., Lozano, R.P., Isanta, N., Hellstrom, J., 2010. Manganese stromatolites in caves: el Soplao (Cantabria, Spain). Geology 38, 1119–1122.
Rossi, C., Mertz-Kraus, R., Osete, M.L., 2014. Paleoclimate variability during the Blake

geomagnetic excursion (MIS 5d) deduced from a speleothem record. Quat. Sci. Rev. 102, 166–180.
Rossi, C., Vergara, M.Y., Pradana, R.J., 2017. Porosity-permeability relationships in the Reocín Fm dolostones (La Florida mines-El Soplao cave, Cantabria). I congreso científico internacional de cuevas y minas "El Soplao" 405–416.
Sinclair, D.J., Banner, J.L., Taylor, F.W., Partin, J., Jenson, J., Mylroie, J., Goddard, E., Quinn, T., Jocson, J., Miklavič, B., 2012. Magnesium and strontium systematics in tropical speleothems from the Western Pacific. Chem. Geol. 294–295, 1–17.
Smith, A.C., Wynn, P.M., Barker, P.A., Leng, M.J., Noble, S.R., Tych, W., 2016a. North Atlantic forcing of moisture delivery to Europe throughout the Holocene. Sci. Rep. 6, 24745.
Smith, A.C., Wynn, P.M., Barker, P.A., Leng, M.J., Noble, S.R., Stott, A., 2016b. Cave monitoring and the potential for palaeoclimate reconstruction from Cueva de Asiul, Cantabria (N. Spain). Int. J. Speleol. 45 (1), 1–9.
Spötl, C., Fairchild, I.J., Tooth, A.F., 2005. Cave air control on dripwater geochemistry, Obir Caves (Austria): implications for speleothem deposition in dynamically ventilated caves. Geochem. Cosmochim. Acta 69, 2451–2468.
Steffensen, J.P., Andersen, K.K., Bigler, M., Clausen, H.B., Dahl-Jensen, D., Fischer, H., Goto-Azuma, K., Hansson, M., Johnsen, S.J., Jouzel, J., Masson-Delmotte, V., Popp, T., Rasmussen, S.O., Röthlisberger, R., Ruth, R.U., Stauffer, B., Siggaard-Andersen, M.-L., Sveinbjörnsdóttir, A.E., Svensson, A., White, J.W.C., 2008. High-resolution Greenland Ice Core data show abrupt climate change happens in few years. Science 321, 680–684.
Stoll, H.M., Moreno, A., Mendez-Vicente, A., Gonzalez-Lemos, S., Jimenez-Sanchez, M., Dominguez-Cuesta, M.J., Edwards, R.L., Cheng, H., Wang, X., 2013. Paleoclimate and growth rates of speleothems in the northwestern Iberian Peninsula over the last two glacial cycles. Quat. Res. 80, 284–290.
Tan, M., Baker, A., Genty, D., Esper, J., Cai, B., 2006. Applications of stalagmite laminae to palaeoclimate reconstructions: comparison with dendrochronology/climatology. Quat. Sci. Rev. 25, 2103–2117.
Tremaine, D.M., Froelich, P.N., 2013. Speleothem trace element signatures: a hydrologic geochemical study of modern cave dripwaters and farmed calcite. Geochimimica et Cosmochimica Acta 121, 522–545.
von Grafenstein, U., Erlenkeuser, H., Brauer, A., Jouzel, J., Johnsen, S.J., 1999. A mid-European decadal isotope-climate record from 15,500 to 5000 years BP. Science 284, 1654–1657.
Wong, C.I., Banner, J.L., Musgrove, M., 2011. Seasonal dripwater Mg/Ca and Sr/Ca variations driven by cave ventilation: implications for and modeling of speleothem paleoclimate records. Geochem. Cosmochim. Acta 75, 3514–3529.